**Link sito dell'editore**: https://www.springer.com/journal/10800

**Link codice DOI**: 10.1007/s10800-017-1088-8

**Citazione bibliografica dell'articolo:**

C. Mele, A. Bilotta, P. Bocchetta, B. Bozzini. *Characterization of the particulate anode of a laboratory flow Zn-air fuel cell*. Journal of Applied Electrochemistry, 47 (2017) 877-888.

# Characterization of the particulate anode of a laboratory flow Zn-air fuel cell

Claudio Mele[1,*], Angelo Bilotta[2], Patrizia Bocchetta[1] and Benedetto Bozzini[1]

[1]Dipartimento di Ingegneria dell'Innovazione, Università del Salento, via Monteroni, I-73100 Lecce - Italy

[2]Argo s.r.l., Via delle Grigne, 25 – I-20090 Segrate (MI) - Italy

*Corresponding author: claudio.mele@unisalento.it, tel.: 0039 0832 297621, fax: 039 0832 297621

## Abstract

A tapered-end flow Zn-air fuel cell (ZAFC), mechanically refuelable with Zn micro-spheres, was employed to study the effect of KOH electrolyte aging on the Zn anode. A complete description of the architecture of the adopted cell is reported. The electrochemical characterization of the ZAFC was performed by long-term current discharge tests in galvanostatic mode: the corresponding polarization and power density curves were plotted. An insightful investigation on the particulate Zn anode consisting of spheres of diameter 0.4 mm was performed by means of X-ray diffraction (XRD), scanning electron microscope (SEM) and Raman spectroscopy in order to characterize the crystallographic structure, surface morphology and chemical nature of residual metal and solid corrosion products. Electrochemical impedance spectroscopy (EIS) allowed to obtain information on the charge transfer mechanism of zinc anode reaction and on the thickness, compactness, and blocking features of the passive film as a function of the ageing of the electrolyte. The results of our analysis revealed the formation of a passive layer of zinc consisting of a white and porous film of ZnO precipitate (type I) and a light-gray to black compact film (type II). The failure of the particulate anode was chiefly caused by the increase in zincate concentration in the electrolyte, but

is was enhanced by the non-uniform spatial current distribution due to the instability of the passive film at high pH.

**Keywords:** Zn-air fuel cell; Alkaline electrolyte; Raman; Electrochemical impedance spectroscopy

## 1. Introduction

Among the configurations for Zn-air rechargeable batteries, mechanically and electrically rechargeable systems generated significant interest as next-generation battery for automotive and stationary applications [1-3]. Mechanically rechargeable Zn-air fuel cells (ZAFCs) can be categorized into two types, "reconstructable cells" and "refuelable cells" [4, 5]. In the former case, Zn plates or cassettes are replaced and are designed to be physically removed and regenerated after discharging. In the latter case of "refuelable cells", aqueous electrolytes are pumped into the battery, either carrying Zn electroactive fuel or flowing the electrolyte through a packed bed of Zn particles that progressively corrode and are discharged by gravity. Several approaches for ZAFCs anode have been proposed by different research groups and summarized in several reviews (i.e. [5, 6]): a system with mechanically refuelable anode [1], a fluidized bed system [2] and a tapered-end structure [7, 8].

In terms of Zn electrode failure, in the case of mechanically rechargeable Zn-air fuel cells, passivation and self-discharge are two of the main problems responsible for poor cycle life performance [6]. Since solid Zn and zinc oxide (ZnO) particles are handled in a ZAFC, the clogging problem of unreacted zinc, solid products and byproducts in the electrolyte is quite severe. In the packed-bed anode configuration described in [9, 10] the electrolyte flows by natural convection and bed occlusion limit the cell capacity and performance. Some of the research works to solve this problem were conducted in a fluidized bed system [2], but unreacted zinc still remained in this case. According to literature packing and clogging in the bed could be prevented by a tapered-end

structure of the anode [7, 11, 12], where the formation of bridges and voids between the Zn particles allow the electrolyte to circulate easily with low hydraulic resistance. In this configuration the Zn particles compartment is made of two non-parallel surfaces with a small vertical angle served by a continuous vertical flow of electrolyte. The distance between walls must be designed to promote bridging of the particles, typically about 1 to 7 times the average dimensions of the particles at the point of entry into the cell [7, 13]. The anodic dissolution of Zn under discharge progressively reduces the size of the reacting particles that move downwards by gravity together with solid products and byproducts. The tapered geometry allows the gap/particle size ratio to be maintained as the particles travel from the top to the narrower end at the bottom of the anodic compartment. Accordingly, a low packing density and a low hydraulic resistance are guaranteed in the particle bed thanks to the formation of particle arches and/or bridges between the nonparallel walls promoting the development of voids during subsequent particle dissolution.

In this work we adopted a mechanically refuelable tapered-end flow Zn-air fuel cell with Zn micro-spheres fuel ([6, 14] and reference therein) and we studied the effect of electrolyte aging on the behaviour of the Zn anode. An insightful characterization the Zn anode spheres by means of EIS, SEM, EDX and Raman measurements, not yet available in literature, is provided together with a complete description of a simple tapered cell architecture aimed to facilitate the reproducibility of future experiments on flow Zn-air cells using Zn microspheres.

## 2. Experimental

### *2.1 Cell architecture*

In this work we adopted a mechanically refuelable flow ZAFC concept, based on the tapered-end device described in [6, 14] and we have carried out our studies on a self-fabricated laboratory device [15]. The cell was constructed by assembling two components of polymethyl metacrylate

(PMMA), a hopper on the anodic side and a gas distribution plate on the cathodic side, hosting the current collector and the air cathode. The anode consisted of Zn spheres having diameter of 0.4 mm, that were fed into the anode chamber through the hopper. The exposed area of a sphere inside an assembly with varying packing ratio is not easy to be calculated. In agreement with [16], we have estimated the theoretical surface area of the anode by assuming that the spheres were cubes with 1/6 (one face) of their surface area inaccessible either because they attach to the substrate or because they attach to another particle. Based on the initial number of Zn spheres (46878) and considering the area of a single micro-sphere ($0.02 cm^2$) the theoretical surface area is calculated to be 780 $cm^2$. Driven by gravity, Zn spheres automatically flowed from the upper end to the lower end of the anode chamber. To reduce the self-discharge problem, a copper current collector having high hydrogen overpotential was employed [17]. Potassium hydroxide (KOH) 6 M was selected as electrolyte because of its good conductivity [5, 18]. KOH was contained in a separated storage tank and was degassed by nitrogen in order to reduce the problem of the formation of carbonate. In fact $CO_2$ present in the air dissolves in the electrolyte forming carbonate and, consequently, increasing the viscosity of the electrolyte and decreasing its ionic conductivity [6]. KOH was then pumped into the chamber, by means of a peristaltic pump, producing a circulating flow from the bottom to the top of the hopper. The electrolyte flow rate was set at 1 liter per hour. The air electrode was soaked in KOH solution for 6 hours before use in the cell [9, 19]. The cathode was an Electric Fuel E-4 Air Electrode consisting in three layers: an active layer of manganese based catalyzed carbon, a blocking layer of laminated porous Teflon film and a separator layer of laminated microporous film with non-woven fabric. Oxygen was fed fluxing in a gas distribution plate (**Fig. 1**) at a rate of $10^{-3}$ liter per hour and reduced to hydroxyl ions, completing the discharging process.

### *2.2 Electrochemical characterization of the Zn-air battery*

The electrochemical characterization (current discharge test, polarization and power density curves) of the Zn-air battery was performed, at room temperature, at the constant current of 212 mA (or 7

mA $cm^{-2}$ with respect to the air cathode area) by means of an AMEL 5000 potentiostat/galvanostat. A single current discharge test at 750 mA (or 25 mA $cm^{-2}$) was also performed.

EIS measurements were carried out through a Parstat 2273 potentiostat/galvanostat equipped with an Impedance Analyzer directly connected to the cell. The impedance spectra were recorded in the range 2 MHz- 0.01 Hz at 25 °C and an ac amplitude of 10 mV. Before each measurement, the cell was stabilized for at least 15 min. The high frequency inductive points were not considered because they do not convey electrochemical information, but are rather determined by the porous nature of the electrodes and to the electronic contacts of the cell [20, 21]. The data analysis and equivalent circuit fitting were carried out through the EIS Spectrum Analyzer software. The function selected to minimize the difference between the experimental and theoretical data is based on the amplitude weighting:

$$r_c^2 = \sum_{i=1}^{N} \frac{\left(z_i^{'} - z_{i_{calc}}^{'}\right)^2 + \left(z_i^{''} - z_{i_{calc}}^{''}\right)^2}{z_i^{'2} + z_i^{''2}} \qquad (1)$$

where i corresponds to measured values of impedance and $i_{calc}$ corresponds to the calculated values and N is the number of points.

### *2.3 Characterization of the spent zinc spheres anode*

After the long-term current discharge test, we disassembled the cell for visual observation and we characterized the spent zinc spheres for their crystallographic structure, surface morphology and chemical nature by means of XRD, SEM and Raman spectroscopy, analyzing three samples of powder at three different locations along a channel of the hopper in the anodic side of the cell. XRD analyses were performed by means of a Ultima+Rigaku diffractometer, equipped with a Bragg–Brentano goniometer. The surface morphology was examined with a Cambridge Stereoscan SEM. Raman measurements were performed with a LabRam confocal system, using a 10x objective. Excitation at 633 nm was provided by a He–Ne laser, delivering 7 mW at the sample surface.

## 3. Results and discussion

### *3.1 Electrochemical characterization of the Zn-air battery*

The study was performed introducing an anode, consisting in 25 g of Zn spheres having diameter of 0.4 mm, that were fed into the anode chamber through the hopper. The open circuit potential of the Zn-air battery remained steady at 1.45 ± 0.05 V during 6 h of storage **(Fig. 2)**. **Fig. 3** presents polarization and power density curves for the Zn-air battery. A current density of 56 mA $cm^{-2}$ and a peak power density of 36 mW $cm^{-2}$ were obtained. In this study we are not primarily interested in the peak power delivered by the cell, since this is mainly governed by the performance of the air electrode [22], but rather we concentrate on the depth of discharge, that is instead controlled by the anode performance. **Fig. 4a** presents the discharge characteristics up to a cutoff voltage of 0.2 V at a constant current of 212 mA (7 mA $cm^{-2}$), showing that the discharge was sustained for 91 h (black curve). When normalized to the consumed mass of Zn, the specific capacity of our battery was over 770 mAh $g_{Zn}^{-1}$, corresponding to an energy density of 894 Wh $kg_{Zn}^{-1}$. Slightly lower values of 718 mAh $g_{Zn}^{-1}$, corresponding to an energy density of 673 Wh $kg_{Zn}^{-1}$, have been recorded by applying a current of 750 mA (25 mA $cm^{-2}$). Furthermore, no significant potential drop was observed under galvanostatic discharge for about 24 h (**Fig. 5**).

With the adopted system, although Zn is gradually consumed during the discharge process, after discharge battery operation can be resumed by refilling the Zn spheres. Therefore, after the discharge at a cutoff voltage of 0.2 V, the battery was mechanically recharged introducing 25 additional grams of Zn spheres and the discharge characteristics at a constant current of 212 mA (7 mA $cm^{-2}$) were recorded. Discharge and mechanical recharge were repeated five times. In order to evaluate the effect of the KOH electrolyte ageing, the same electrolyte, having a volume of 5 liter was continuously flushed. In correspondence of the fifth recharge we noticed a clear decrease in the discharge time and consequently in the specific capacity due to the aging of the electrolyte driven

by the electrochemistry of zinc in concentrated alkaline solutions. Alkaline zincate solution can be reasonably treated as a ternary electrolyte consisting of KOH, potassium zincate ($K_2Zn(OH)_4$), and $H_2O$ [23]. When ionic zinc species $Zn^{2+}$ are introduced into the solution by dissolution of Zn [24-26]:

$$Zn + 4\ OH^- \rightarrow Zn(OH)_4^{2-} + 2e \qquad (2)$$

they may remain in the electrolyte as zincate ions or deposit as $ZnO_{(s)}$:

$$Zn(OH)_4^{2-} \rightarrow ZnO_{(s)} + 2\ OH^- + H_2O \qquad (3)$$

In addition, $Zn(OH)_4^{2-}$ ions can also precipitate in the form of solid $K_2Zn(OH)_4$ if the solution is oversaturated with $K_2Zn(OH)_4$. Both solid ZnO and solid $K_2Zn(OH)_4$ are electrical insulators and have higher molar volumes than metallic zinc; consequently, their precipitation in a zinc electrode may cause pore blockage in addition to electrode passivation, gradually decreasing the specific capacity of the cell. The relevant precipitation rates depend on alkali concentration (decreasing during discharge), initial electrode porosity, and applied current density.

Therefore, after the 5$^{th}$ recharge, in addition to the usual addition of 25 g of Zn spheres, we replaced the spent electrolyte with a fresh one. We recorded the discharge characteristics at 212 mA (7 mA cm$^{-2}$), and then we repeated a second time this operation of addition of zinc and fresh electrolyte. In this case we observed better discharge characteristics with respect to the fifth recharge that we discussed before. Furthermore we noticed that, as expected, with fresh flowing electrolyte, the general degradation trend is clearly slower than in the case of recirculation of the same electrolyte for several complete discharge cycles. We quantified this behavior in terms of current efficiency (**Fig. 4b**).

The flux of the electrolyte under discharge is a necessary condition to allow the regeneration of cell by means of electrolyte renewing. In fact, if the same battery is discharged in stagnant condition, its performance is dramatically degraded. In **Fig. 6** we report six discharge characteristics to a cutoff voltage of 0.2 V at a constant current of 212 mA (7 mA cm$^{-2}$) recorded without flux of KOH

solution. One can easily observe that the depth of the first discharge is one order of magnitude less with respect to the one of the fluxed cell (**Fig. 4a**), furthermore this value cannot be recovered by adding fresh electrolyte due to the irreversible and drastic packing and clogging of the Zn spheres [27]. The sudden drop in the voltage observed in correspondence of each new charge was caused by a sudden increase in current density after leaving the battery at the open circuit potential [19]

### *3.2 Characterization of the Zn spheres anode*

#### *3.2.1 In-situ EIS study*

Electrochemical Impedance Spectroscopy (EIS) has been used to monitor the anodic behaviour of the Zn spheres. To this aim, the impedance of the Zn-air cell as function of applied potential, state-of-charging (SoC) and number of mechanical charging steps has been studied.

**Fig. 7a** reports the EIS Nyquist plots of the Zn-air cell at different applied potentials. The low frequency arc generally attributed to the air cathode ORR charge transfer [28] is visible and decreases in diameter with increasing applied cell potential, whereas the high frequency impedance data, typically referred to the anode impedance, have a poor signal-noise ratio. Therefore, the individual spectral contributions of the two electrodes cannot be clearly resolved, and the separation of the fitting parameters using a model involving two separated electrodes requires assumptions with questionable validity [29]. For this reason, the particulate Zn anode the has been studied separately by using a three electrode configuration with an Ag/AgCl reference inserted in the anodic compartment. Potentiostatic EIS Nyquist plots at fixed anodic potentials between 0 and 100 mV vs. OCP have been recorded at SoC=100% in fresh (1$^{st}$ discharge curve) (**Fig. 7b**) and aged (4$^{th}$ discharge curve) (**Fig. 7c**) zincate solutions. In both conditions the impedance spectra has been fitted according to the equivalent circuit shown in the inset of **Fig. 7b** [30, 31]. In the model, $R_{ohm}$ represents the ohmic resistance, i.e. the intercept of the impedance spectra at high frequency with the real axis, associated with uncompensated contact and electrolyte resistance [32], $R_{ct}$ corresponds to the anodic charge transfer resistance, $CPE_{ct}$ is the double layer capacitance, $R_{film}$ and $CPE_{film}$ are

the resistance and capacitance of the zinc oxide film on the metal surface. The non ideal capacitive behavior is related to many factors such as roughness and fractal geometry, electrode porosity and to current and potential distributions related with irregular electrode geometry and heterogeneities [33]. A circuit model that takes into account the impedance properties of the zinc oxide film during the charge transfer across the film should be physically more significant, also considering that an oxide film is formed immediately upon exposing the zinc electrode to the air [30]. On the basis of this equivalent circuit, the fit parameters values has been determined with good $r_c^2$ values (see Experimental Section and **Fig. 7**) and relative errors less than the 10 % and shown in **Fig. 8.**

As reported in **Fig. 8a**, the $R_{ohm}$ remains almost constant with the anodic polarization for fresh solution as expected for an ohmic behavior. Taking into account the distance of 0.2 cm between the reference electrode and the anode and the nominal surface area of 30 $cm^2$, a value of conductivity of 660 mS $cm^{-1}$ can be estimated in very good agreement with the conductivity of 6 M KOH (ca. 620 mS $cm^{-1}$ reported in [25]). However, the electrolyte resistance increases when the solution contains more zincate ions coherently with the ionic conductivity of KOH/Zincate solutions [25].

The charge transfer resistance ($R_{ct}$) of zinc anode reaction shown in **Fig. 8b** depends on the overpotential in agreement with the Tafel equation [34] both in fresh and in aged electrolyte, corresponding to a more concentrated zincate solution, confirming the adequacy of the model. In order to compare the double layer capacitance values of the two conditions we cannot rely solely on the values of CPE since the dimension of CPE ($s^n$/ohm) depends on the value of the exponential factor n, that can change across the performed measurement. Thus, an estimation of the double layer capacitance ($C_{DL}$) has been made from the $CPE_{DL}$ values by using the equation $C_{DL} = CPE_{DL} \cdot (w_{max})^{1-n}$ proposed in [35, 36] (**Fig. 8c)**. For a fresh solution $C_{DL}$ exhibits an almost constant value of 9.46 mF/$cm^2$ (by considering the effective geometric surface of the Zn spheres anode of 780 $cm^2$ (see Experimental Section)), a value comparable with literature data on analogous systems [25, 37]. In concentrated zincate solution the trend of the $C_{DL}$ can be correlated to that of the parameter n

shown in **Fig. 8d**. In diluted conditions the $C_{DL}$ values are the same as the ones measured under OCP conditions whereas, at 30 mV vs OCP, they increase by one order of magnitude at the anodic potential where the CPE becomes a pure capacitance (n=1, **Fig. 8d**): for higher anodic polarizations $C_{DL}$ values decrease with some fluctuations. From the $C_{DL}$ behavior and from the $n_{DL}$=1 values it can be deduced that the space charge region is very much flattened, i.e. parallel plate capacitance, indicating reaction only through a smooth surface. In presence of high concentrations of zincate, the compaction of the surface can be related to the formation of a passive film that decreases the porosity and leakage between the Zn spheres [31].

In a fresh solution the film resistance ($R_{film}$) is quite low and constant with anodic polarization, because the high pH, maintained by the electrolyte flow, hinders passivation. When the zincate concentration increases to values close to saturation and pH decreases, passivation is expected to occur, forming an inner light gray/black dense ZnO layer in the region closer to the anode surface at the metal/electrolyte interface, favored by the lower pH, and an external white porous layer by precipitation of saturated zincate ions ($Zn(OH)_4^{2-}$) [26, 38, 39] (**Fig. 9**). In this case the $R_{film}$ was found to decrease with the anodic overpotential (**Fig. 8e**), suggesting a field-enhanced dissolution and/or modifications of composition, morphology and thickness of the ZnO passive layer, that has been reported to be dependent on the anodic potential [40].

The anodic discharge curve has also been measured simultaneously with that of the cell at 7 mA $cm^{-2}$ and reported in **Fig. 10a**. From this Figure we can infer that the decrease of cell potential with time can be mainly attributed to the anodic overpotential. The increase of the anodic overpotential with time of discharge can be attributed to the decrease of anodic active area due to zinc consumption and/or to the physico-chemical modifications induced by the Zn passivation occurring at higher zincates concentration (i.e. low SoC).

**Fig. 10b** reports the EIS Nyquist plots of the Zn-air cell at different SoC values. The impedance of the low frequency arc, generally attributed to the ORR charge transfer at the air cathode and to the

diffusion of reacting species through the thin corrosion product film [28, 41], increases with increasing number of discharge steps, suggesting progressive inhibition of mass-transport processes. Nyquist plots of the particulate Zn anode under open-circuit conditions and different SoC values are reported in **Fig. 10c** for the first mechanical charge. The high impedance at SoC=100% can be attributed to intense $H_2$ evolution concomitant with the high corrosion rate of the Zn at OCP due to a high effective area of film-free spheres surface [42]. The ageing of the cell increases the coverage of ZnO film on the Zn surface, thus decreasing the $H_2$ impedance. From SoC=80% (t=17h) to SoC=30% (t=60h), the electrochemical reaction $Zn/Zn^{2+}$ occurs under charge-transfer control at high SoC (80%) values and gradually changes to diffusion control with increasing SoC (30%). The appearance of a diffusion contribution to impedance can be due to the development of the passive layer on the zinc spheres and/or other insoluble complexes, resulting from the increased concentration of zincate in the electrolyte with increasing depth of discharge. Hydroxide ions have to diffuse through this passive layer to react with zinc ions and the kinetics of the reaction is thus controlled by the diffusion through the passive film of $OH^-$ ions to reaction sites and of oxidation products away from it. Precipitation followed by zinc oxidation, dissolution and diffusion in the electrolyte during discharge easily brings about passivation [43, 44]: in our cell these processes are hindered by the flow of electrolyte (as evidenced by the comparison between **Fig. 4a** and **6**). The increase of zincate concentration has a growing impact on the voltage output and current efficiency, that gradually decrease from the 1$^{st}$ to the 5$^{th}$ curve as shown in **Fig. 4a** and **4b.** The 5$^{th}$ mechanical recharge marks the end of the useful life of the electrolyte, due to zincate saturation; in fact by renewing the electrolyte in the same cell (6$^{th}$ curve in **Fig. 4a**), the discharge curve notably improves. Nevertheless the same output voltage (decrease of 7 %) and current efficiency (**Fig. 4b)** of the 1$^{st}$ charge cannot be recovered. This is also confirmed by **Fig. 10d** where the EIS spectra of the 1$^{st}$ and 7$^{th}$ charge are compared: the diffusion control due to passive film formation discussed above appears at lower SoC values (SoC= 80%, 17 h) for the 7$^{th}$ mechanical charge. This suggests

that the ageing of the anode during discharge cannot be associated only with the ageing of the electrolyte. In fact, the use of concentrated alkaline solutions (such as 6 M KOH) and the flow of the electrolyte reduce zinc passivation because of the partial dissolution of the passive film [26]. However, excessively high solubility generates morphological changes of the anode surface at preferential sites that in turn cause non-uniform current distribution leading to undesirable electrolyte concentration gradients [25]. As a consequence, un-reacted inactive Zn/ZnO spheres are accumulated at the end of every discharge, as demonstrated by the different morphochemical features of the Zn spheres observed along the longitudinal dimension of the cell discussed in the Section 3.1.2.

*3.2.2 Characterization of spent zinc spheres*

After the 7$^{th}$ discharge of the long-term current discharge test at 212 mA (7 mA cm$^{-2}$), we characterized the spent zinc spheres for their crystallographic structure, surface morphology and chemical nature by means of SEM, XRD and Raman spectroscopy, analyzing three samples of the residual powder at three different locations along one channel of the hopper in the anodic side: close to the inlet of the flow-field, mid-way between the inlet and the outlet and close to the outlet, as indicated in **Fig. 11a**.

- *XRD*

The XRD patterns of the spent zinc samples taken from the three indicated positions, as described above, are reported in **Fig. 11b** and compared to those of fresh zinc particles. As expected and coherently with the JCPDS card 04-0831, the fresh zinc displayed characteristic peaks of Zn metal, at 2θ of 36.4, 39.0, 43.4, 54.5, 70.4, 77.4, 82.3, 86.6, 90.3 and 95.0°. The residual powder collected from positions A, B and C after the long-term current discharge test, shows different patterns. The material found in zone C shows the peaks of Zn metal described above, together with the characteristic peaks of ZnO, according to the JCPDS card 36-1451, at 2θ of 31.8, 34.4, 36.2, 47.5, 56.5, 62.8, 66.4, 68.0, 69.0, 72.6, 77.0, 81.4, 89.7, 92.8, 95.4 and 98.7°. Material from zones A and

B shows only the peaks corresponding to ZnO. No traces of zinc metal are visible. The obtained results are coherent with anode reactions (2) and (3).

Initially, zinc metal is oxidized to release electrons and form zinc(II) ions. This process proceeds until the concentration of the zincate ions, $Zn(OH)_4^{2-}$, reaches saturation. In the saturated solution zincate ions further react forming solid ZnO. In the experiments carried out with flowing electrolyte, instead, zincate ions are continuously carried along the channel and their concentration progressively increases. This situation favours the formation of ZnO in the upper part of the channel. Instead the presence of metal Zn in zone C was due to a not yet complete oxidation of Zn spheres present in this area, where the Zn particle layer lies far from the anodic current feeder.

- *SEM*

**Fig. 11c** shows the SEM images of pristine zinc spheres and of the three samples of the residual zinc powder recovered from the anode hopper after the long-term discharge test. The fresh zinc spheres present a smooth surface while, coherently with the literature [45-47], two different kinds of ZnO morphology can be observed on the one hand for zone C and on the other hand for zones B and A, respectively. The black reaction product present in zone C appears as a compact film, whereas the grey material formed in zone B and the white one found in zone A show a porous morphology.

- *Raman*

The Raman spectra of the spent zinc powder at the three different investigated locations are reported in **Fig. 11d**. In all the spectra six more evident peaks can be observed: at 333, 378, 406, 439, 574 and 584 $cm^{-1}$. All these peaks, together with the peak at 99 $cm^{-1}$ - not visible from the performed measurements, because it is outside the range of the collected spectra - are the typical Raman peaks of ZnO. In fact, on the basis of literature data, the Raman spectrum of ZnO presents 6 peaks, corresponding to the following modes: $A_1$ (TO) at 378 $cm^{-1}$ and $A_1$ (LO) at 574 $cm^{-1}$, $E_1$ (TO) at 406 $cm^{-1}$ and $E_1$ (LO) at 584 $cm^{-1}$ are polar modes associated to the oxygen-dominated

phonons, whereas the peaks at 439 $cm^{-1}$ and 330 $cm^{-1}$ attributed to $E_2^{high}$ and to the combination $E_2^{high}$ - $E_2^{low}$, respectively, are non-polar modes [48, 49]. The spectra obtained on the powder in the three different locations of a channel of the hopper, reveal that moving from zone A to zone C, the intensity of the Raman band at 574 $cm^{-1}$, corresponding to the $A_1$ (LO) mode, markedly increases, whereas the band at 439 $cm^{-1}$, corresponding to $E_2^{high}$ mode decreases. The changes between the intensities of these two peaks and in particular the presence of a high intensity one corresponding to the $A_1$ (LO) mode can be attributed to the presence of interstitial Zn and oxygen deficiency in the lattice ($Zn_{1+x}O$), as already observed in the past for ZnO film obtained by electrochemical passivation in alkaline solution [50, 51] or sputtering under high vacuum conditions [52, 53]. This result is also confirmed by the dark color of zone A. In fact the darkening of the film has been ascribed to the incorporation of an excess of zinc within the lattice structure of zinc oxide [54].

The conclusions that can be drawn from the analysis of our Raman and SEM data on anodically formed ZnO that are coherent with the structure of the passive layer of zinc observed by [51, 55], i.e. a dual layer structure consisting of a porous film of ZnO precipitate (type I) and a compact film (type II), and shown in **Fig. 9.** Type I is white and porous and forms by precipitation from a supersaturated layer of electrolyte and Type II forms directly on the electrode surface and ranges from light-gray to black due to an excess of zinc in the film. The formation of type II film is favored by low pH at the interface between the metal and the electrolyte and contributed to the failure of the Zn anode to operate properly by blocking the diffusion of $OH^-$ ions toward Zn interface in agreement with EIS results shown in **Fig. 10d**. The results of this work have shown that the failure of the anode spheres is mainly due to electrolyte ageing (increase in zincate concentration) as expected (**Fig. 4a**, 5$^{th}$ curve), but another component of degradation comes from a non-uniform spatial current distribution due to the instability of the passive film at high pH (6M KOH), with the presence of voids detected at the compact oxide/precipitated layer interface and within the compact

oxide itself (**Fig. 9)** [26] and revealed by analyzing the morphochemical distribution of ZnO along the longitudinal dimension of the anode.

## 4. Conclusions

This work reports a detailed study of the effect of electrolyte aging during battery discharge on the behaviour af the particulate Zn anode of a mechanically refuelable tapered-end flow Zn-air fuel cell. The potential decrease in the Zn-air battery discharge curve is mainly due to the anodic overpotential increase. By means of EIS measurements, this effect has been attributed to the physico-chemical modifications induced by the Zn passivation occurring at higher zincates concentration (i.e. low SoC). The EIS spectra of the anode spheres recorded under anodic polarization revealed that the impedance properties of the zinc oxide film and the charge transfer parameters can be easily separated and quantified. The charge transfer resistance of zinc anode reaction depends on the overpotential in agreement with the Tafel equation, while qualitative variations in thickness, compactness, and blocking features of the passive film as a function of the ageing of the electrolyte (i.e SoC) can be also obtained. In particular, the electrochemical reaction $Zn/Zn^{2+}$ occurs under charge-transfer control at high SoC (80%) values gradually changes to diffusion control with the decrease of the SoC (30%), due to the development of the passive layer on the zinc spheres and/or other insoluble complexes owing to the increased concentration of zincate in the electrolyte. The results of this work have thus shown that the failure of the anode spheres is mainly due to electrolyte ageing (increase in zincate concentration). Moreover, another component of degradation coming from a non-uniform spatial current distribution, due to the instability of the passive film at high pH (6M KOH), with the presence of voids at the compact oxide/precipitated layer interface and within the compact oxide itself, has been revealed by analyzing the morphochemical distribution of ZnO along the longitudinal dimension of the anode by means of XRD, SEM and Raman measurements. As a consequence, unreacted inactive Zn/ZnO

spheres are accumulated at the end of every discharge step. The analysis of our Raman and SEM data are coherent with the dual layer structure consisting of a porous film of ZnO precipitate (type I) and a compact film (type II)**.** The formation of type II film is favored by low pH at the interface between the metal and the electrolyte and contributed to the failure of the Zn anode by blocking the diffusion of $OH^-$ ions toward Zn interface in agreement with EIS results.

**References**

[1] Goldstein J, Brown I, Koretz B (1999) New developments in the Electric Fuel zinc-air system. J Power Sources 80:171-179

[2] Smedley S (2000) Zinc Air Fuel Cell for Industrial and Specialty Vehicles. IEEE Aerosp Electron Syst Mag 15:19-21

[3] Schröder D (2016) Analysis of Reaction and Transport Processes in Zinc Air Batteries. Springer Vieweg p. 178

[4] Cooper JF, Fleming D, Keene L, Maimoni A, Peterman K, Koopman R (1994) Demonstration of Zinc/Air Fuel Battery to Enhance the Range and Mission of Fleet Electric Vehicles: Preliminary Results in the Refueling of a Multicell Module

[5] Xu M, Ivey DG, Xie Z, Qu W (2015) Rechargeable Zn-air batteries: Progress in electrolyte development and cell configuration advancement. J Power Sources 283:358-371

[6] Sapkota P, Kim H (2009) Zinc-air fuel cell, a potential candidate for alternative energy. J Ind Eng Chem 15:445-450

[7] Cooper JF (1995) Continuos-feed electrochemical cell with nonpacking particulate electrode. US Patent 5,434,020

[8] Pinto M, Smedley S, Colborn JA (2004) US Patent 6,706,433 B2

[9] Evans JW, Savaskan G (1991) A Zinc-Air Cell Employing a Packed Bed Anode. J Appl Electrochem 21:105-110

[10] Savaskan G, Huh T, Evans JW (1992) Further studies of a zinc-air cell employing a packed bed anode part I: Discharge. J Appl Electrochem 22:909–915

[11] Pei P, Ma Z, Wang K, Wang X, Song M, Xu H (2014) High performance zinc air fuel cell stack. J. Power Sources 249:13-20

[12] Sapkota P, Kim H (2010) An experimental study on the performance of a zinc air fuel cell with inexpensive metal oxide catalysts and porous organic polymer separators. J Ind Eng Chem 16:39-44

[13] Abrams A (1977) Mud Design to Minimize Rock Impairment Due to Particle Invasion. J Petrol Technol 29:586-592

[14] Cooper JF, Krueger R (2006) The Refuelable Zinc-Air Battery: Alternative Techniques for Zinc and Electrolyte Regeneration

[15] Bozzini B, Altissimo M, Amati M, Bocchetta P, Gianoncelli A, Gregoratti L, Kourousias G, Mancini L, Mele C, Kiskinova M (2015) In Situ and Ex Situ X-Ray Microspectroelectrochemical Methods for the Study of Zinc-Air Batteries. Elsevier Reference Module in Chemistry, Molecular Sciences and Chemical Engineering. doi:10.1016/B978-0-12-409547-2.11452-0

[16] Fayette M, Nelson A, Robinson RD (2014), Electrophoretic Deposition Improves Catalytic Performance of $Co_3O_4$ Nanoparticles for Oxygen Reduction/Oxygen Evolution Reactions, SI, J Materials Chem A, 4274-4283

[17] Zhang XG (2008) Novel anode for high power zinc-air batteries. ECS Transactions 3:1-11

[18] Mele C, Bozzini B (2015) Spectroelectrochemical investigation of the anodic and cathodic behaviour of zinc in 5.3 M KOH. J Appl Electrochem 45:43-50

[19] Zhang J, Zhao Z, Xia Z, Dai L (2015) A metal-free bifunctional electrocatalyst fro oxygen reduction and oxygen evolution reaction. Nature nanotechnology 10:444-452

[20] Hampson NA, Karunathilaka SAGR Leek R (1980) The impedance of electrical storage cells. J Appl Electrochem 10:3-11

[21] Root MJ (1995) Electrochemical impedance of alkaline zinc/manganese dioxide cells containing no added mercury. J Appl Electrochem 25:1057-1060

[22] Pei P, Wang K, Ma Z (2014) Technologies for extending zinc–air battery's cyclelife: A review. Applied Energy 128:315–324

[23] Mao Z, White RE (1992) Mathematical Modeling of a Primary Zinc/Air Battery. J. Electrochem Soc 139:1105-1114

[24] McLarnon FR, Cairns EJ (1991) The Secondary Alkaline Zinc Electrode. J Electrochem Soc 138:645-664

[25] Mainar AR, Leonet O, Bengoechea M, Boyano I, Meatza I, Kvasha A, Guerfi A, Blázquez JA (2016) Alkaline aqueous electrolytes for secondary zinc–air batteries: an overview. Int J Energy Res 40:1032-1049

[26] Thomas S, Cole IS, Sridhar M, Birbilis N (2013) Revisiting zinc passivation in alkaline solutions. Electrochim Acta 97:192– 201

[27] Li Y, Dai H (2014) Recent advances in zinc–air batteries. Chem Soc Rev 43:5257–5275

[28] Ma H, Wang B (2014) A bifunctional electrocatalyst a-$MnO_2$-$LaNiO_3$/carbon nanotube composite for rechargeable zinc–air batteries. RSC Adv 4:46084-46092

[29] Rodrigues S, Munichandraiah N, Shukla AK (2000) A review of state-of-charge indication of batteries by means of a.c. impedance measurements. J Power Sources 87:12–20

[30] Ko Y, Park SM (2012) Zinc Oxidation in Dilute Alkaline Solutions Studied by Real-Time Electrochemical Impedance Spectroscopy. J Phys Chem C 116:7260−7268

[31] Walkner S, Hassel AW (2014) Combined chemical and EIS study of the reaction of zinc coatings under alkaline conditions. Electrochim Acta 131:130–136

[32] Bidault F, Brett DJL, Middleton PH, Abson N, Brandon NP (2010) An improved cathode for alkaline fuel cells. Int. J Hydrogen Energy 35 (2010) 1783-1788.

[33] Jorcin JB, Orazem ME, Pebere N, Tribollet B (2006) CPE analysis by local electrochemical impedance spectroscopy, Electrochim. Acta 51:1473-1479

[34] Noack J, Cremers C, Bayer D, Tuebke J, Pinkwart K (2014) J Power Sources 253:397-403

[35] Brug GJ, van den Eeden ALG, Sluyters-Rehbach M, Sluyters J (1984) The analysis of electrode impedances complicated by the presence of a constant phase element. J Electroanal Chem 176:275-295

[36] Jovic VD (2003) Determination of the correct value of $C_{dl}$ from the impedance results fitted by the commercially available software. http://www.gamry.com/assets/Application-Notes/Determination-of-Double-Layer-Capacitance-from-a-CPE.pdf

[37] Shivkumar R, Paruthimal Kalaignan G, Vasudevan T (1998) Studies with porous zinc electrodes with additives for secondary alkaline batteries. J Power Sources 75:90–100

[38] Powers RW, Breiter MW (1969) The Anodic Dissolution and Passivation of Zinc in Concentrated Potassium Hydroxide Solutions. J Electrochem Soc 116:719-729

[39] McKubre MCH, Macdonald DD (1981) The Dissolution and Passivation of Zinc in Concentrated Aqueous Hydroxide. J Electrochem Soc 128:524-530

[40] Park HJ, Mao SI (1997) Electrochemical Impedance Spectroscopy and Voltammetry of Zinc in Dilute Alkaline Solutions. Analytical Sciences 13:311-316

[41] Zhuang S, Huang K, Huang C, Huang H, Liu S, Fan M (2011) Preparation of silver-modified $La_{0.6}Ca_{0.4}CoO_3$ binary electrocatalyst for bi-functional air electrodes in alkaline medium, J Power Sources 196:4019-4025

[42] Arisea I, Fukunaka Y, McLarnon FR (2006) Ionic Mass Transfer Accompanying Anodic Dissolution of Zinc in Alkaline Solution. J Electrochem Soc 153:A69-A74

[43] Baugh LM, Higginson A (1985) Passivation of zinc in concentrated alkaline solution-I: characteristics of active dissolution prior to passivation. Electrochim Acta 30:1163–1172

[44] Baugh LM, Baikie AR (1985) Passivation of zinc in concentrated alkaline solution-II: role of various experimental factors and the distinction between the solid-state and dissolution–precipitation mechanisms. Electrochim Acta 1985:1173–1183

[45] Jiratchayamaethasakul C, Srijaroenpramong N, Bunyangyuen T, Arpavate W, Wongyao N, Therdthianwong A, Therdthianwong S (2014) Effects of anode orientation and flow channel design on performance of refuelable zinc-air fuel cells. J Appl Electrochem 44:1205-1218.

[46] Yap CK, Tan WC, Alias SS, Mohamad AA (2009) Synthesis of zinc oxide by zinc-air system. J. Alloys Compd 484 934-938

[47] Cho YD, Fey GTK (2008) Surface treatment of zinc anodes to improve discharge capacity and suppress hydrogen gas evolution. J Power Sources 184:610-616

[48] Damen TC, Porto SPS, Tell B (1966) Raman Effect in Zinc Oxide. Phys Rev 142:570–574

[49] Russo V, Ghidelli M, Gondoni P, Casari CS, Li Bassi A (2014) Multi-wavelength Raman scattering of nanostructured Al-doped zinc oxide. J Appl Physics 115:073508

[50] Cai WB, Scherson DA (2003) In Situ Raman Spectroscopy of Zinc Electrodes in Alkaline Solutions. J Electrochem Soc 150:B217-B223

[51] Hugot-Le Goff A, Joiret S, Saïdani B, Wiart R (1989) In-situ Raman spectroscopy applied to the study of the deposition and passivation of zinc in alkaline electrolytes. J Electroanal Chem 263:127-135.

[52] Exharos GJ, Sharma SK (1995) Influence of processing films on the structure and properties of ZnO films. Thin Solid Films 270:27-32.

[53] Tzolov M, Tzenov N, Dimova-Malinovska D, Pizzuto C, Vitali G, Zollo G, Ivanov I (2000) Vibrational properties and structure of undoped Al-doped ZnO films deposited by RF magnetron sputtering. Thin Solid Films 379:28-36

[54] Armstrong RD, Bell MF (1974) The Electrochemical Behaviour of Zinc in Alkaline solution. In Thirsk HR, Armstrong RD, Bell MF. Electrochemistry, vol. 4. The Royal Society of Chemistry, London, pp. 1–17

[55] Melendres CA (1991) Laser Raman Spectroscopy: Principles and Applications to Corrosion Studies. In: M.G.S. Ferreira, G.A. Melendres. Electrochemical and optical techniques for the study and monitoring of metallic corrosion. Proceedings of the NATO Advanced Study Institute. Vienna do Castelo, Portugal. Springer Science + Business Media Dordrecht, p.367

**Figure captions**

**Fig. 1** - Experimental layout of laboratory Zn-air flow fuel cell used in this work

**Fig. 2** - Open circuit potential of the Zn-air flow fuel cell

**Fig. 3** - Polarization and power density curves of the Zn-air battery

**Fig. 4** - (a) Discharge characteristics of the Zn-air battery at a constant current density of 7 mA $cm^{-2}$ and (b) corresponding current efficiency. At the indicated points, the Zn were mechanically added and the electrolyte was replaced. (c) Scheme of the side-view of the anodic compartment showing non-packed Zn spheres

**Fig. 5** - Specific capacity of the Zn-air battery normalized to the mass of the consumed Zn at constant current density of 7 mA $cm^{-2}$ and of 25 mA $cm^{-2}$

**Fig. 6 –** (a) Discharge characteristics of the Zn-air battery at a constant current density of 7 mA $cm^{-2}$ without flow the electrolyte. (b) Scheme of the side-view of the anodic compartment showing close-packing and clogging of the Zn spheres

**Fig. 7** - Nyquist plots measured before discharge at the bias indicated in the graph and amplitude 10 mV. (a) Cell. WE: Zn spheres anode, RE=CE: air cathode. (b) Anode. WE: Zn spheres anode, RE: Ag/AgCl, CE: air cathode, $1^{st}$ discharge of Fig. 4. (c) Anode. WE: Zn spheres anode, RE: Ag/AgCl, CE: air cathode, $4^{th}$ discharge of Fig. 4. Scatter: experimental points. Line: fitted spectrum. The equivalent circuit used to fit the spectra is reported in the inset of Panel (b)

**Fig. 8** - Variation of impedance parameters obtained by fitting the EIS spectra reported in Figure 7, Panel (b) and (c). (a) ohmic resistance, (b) charge-transfer resistance, (c) double-layer capacitance (d) exponent of the CPE, (e) film resistance

**Fig. 9** - Model of spherical Zn particles with passive ZnO shell

**Fig. 10** - (a) Discharge characteristics of the Zn-air battery and the Zn-spheres anode at a constant current density of 7 mA $cm^{-2}$. Nyquist plots measured at open circuit potential and amplitude 10 mV: (b) WE: Zn spheres anode, CE: air cathode, SoC 100%, (c) WE: Zn spheres anode, RE:

Ag/AgCl, CE: air cathode, 1st discharge of Fig. 4 at various SoC, (d) WE: Zn spheres anode, RE: Ag/AgCl, CE: air cathode, SoC=80%

**Fig. 11** - (a) Spent zinc powder characterized after the long-term current discharge test at the three indicated different locations; (b) XRD diffractograms; (c) SEM micrographs at magnification of 100x and 500x; (d) Raman spectra

## Figures

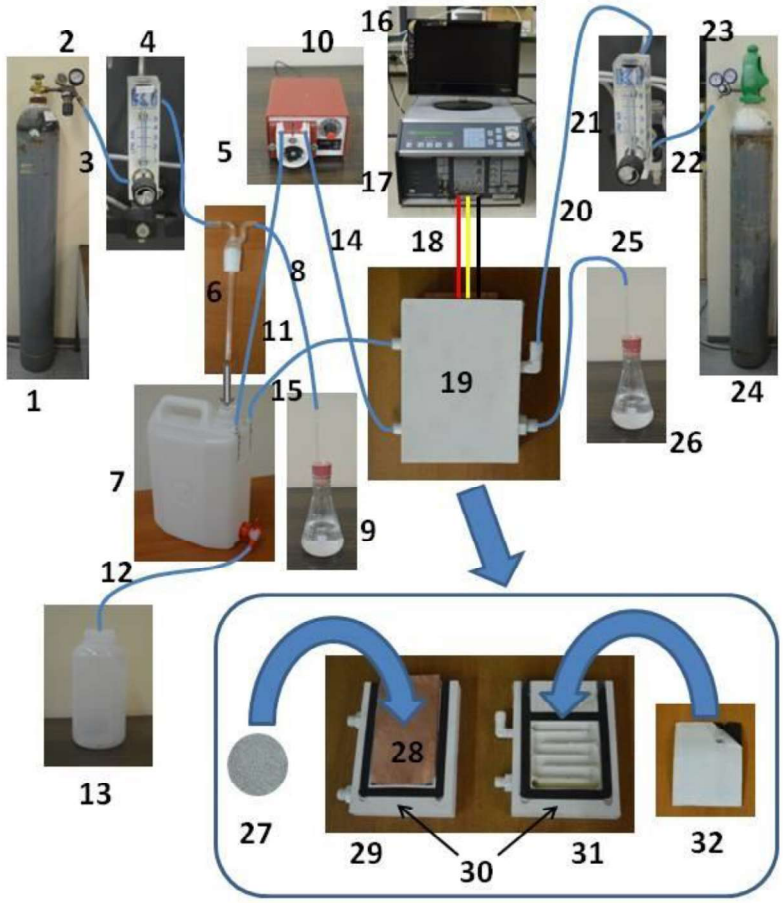


1. Nitrogen cylinder
2. Nitrogen gas flowmeter
3. Tygon tubing R-3603, Ø 6,4 mm
4. Gas flowmeter
5. Tygon tubing R-3603, Ø 6,4 mm
6. Gas bubbler
7. KOH storage tank
8. Tygon tubing R-3603, Ø 6,4 mm
9. Trap for KOH
10. Peristaltic pump
11. Tygon tubing R-3603, Ø 6,4 mm
12. Tygon tubing R-3603, Ø 6,4 mm
13. Drain tank
14. Tygon tubing R-3603, Ø 6,4 mm
15. Tygon tubing R-3603, Ø 6,4 mm
16. PC interfaced with the potentiostat/galvanostat
17. Potentiostat/galvanostat
18. Potentiostat/galvanostat cables
19. PMMA cell
20. Tygon tubing R-3603, Ø 6,4 mm
21. Gas flowmeter
22. Tygon tubing R-3603, Ø 6,4 mm
23. Oxygen gas flowmeter
24. Oxygen cylinder
25. Tygon tubing R-3603, Ø 6,4 mm
26. Trap for checking $O_2$ flow
27. Zinc spheres anode
28. Copper current collector
29. Hopper (anodic side of the cell)
30. Gaskets
31. Gas distribution plate (cathodic side of the cell)
32. Air cathode

**Fig. 1**

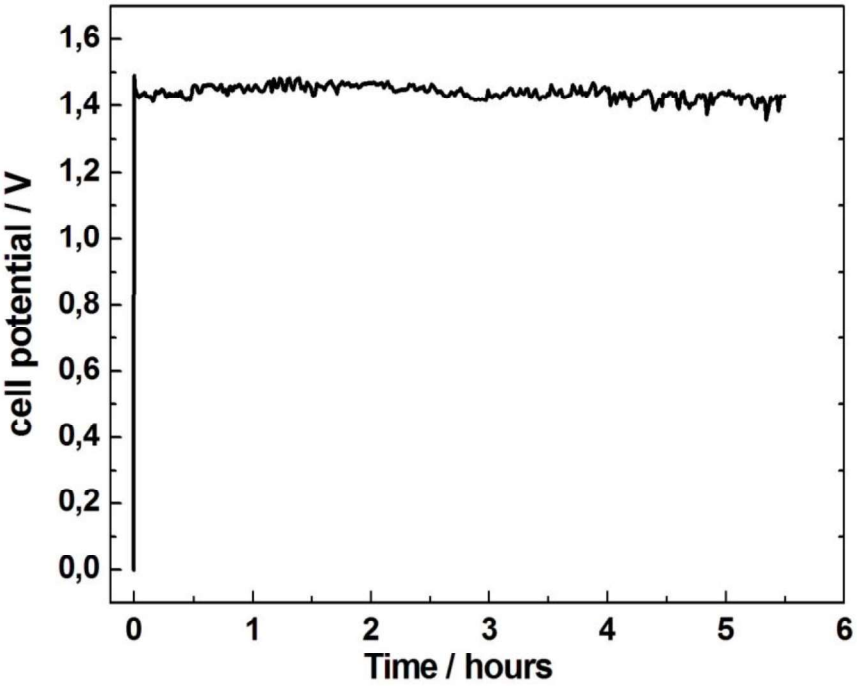


**Fig. 2**

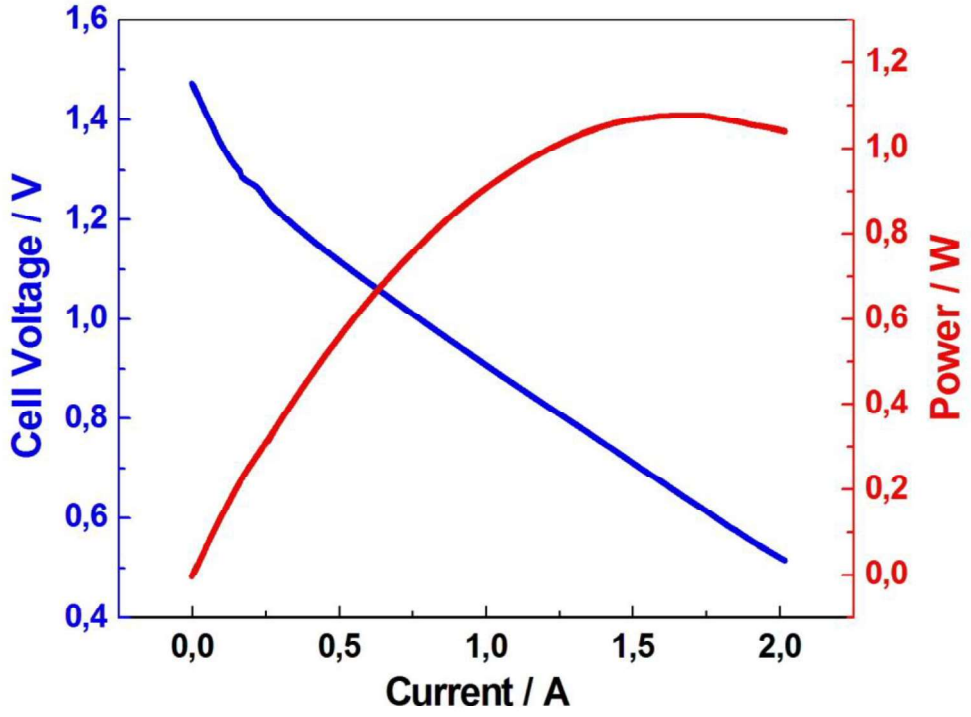
Cell Voltage / V
Power / W
Current / A
1,6
1,4
1,2
1,0
0,8
0,6
0,4
1,2
1,0
0,8
0,6
0,4
0,2
0,0
0,0
0,5
1,0
1,5
2,0

**Fig. 3**

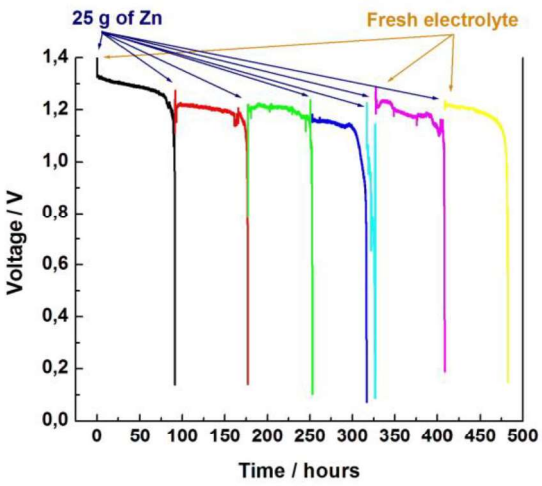
25 g of Zn
Fresh electrolyte
Voltage / V
Time / hours

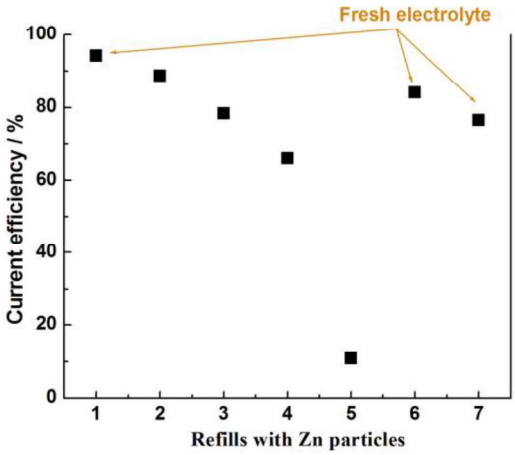
Fresh electrolyte
Current efficiency / %
Refills with Zn particles

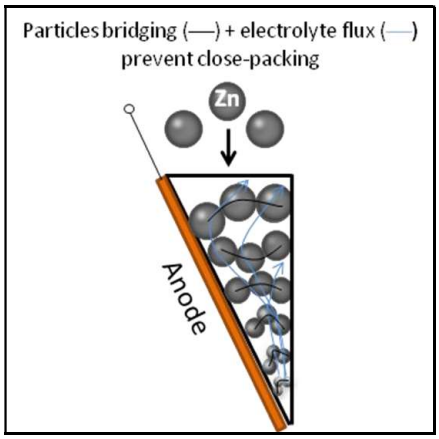
Particles bridging (—) + electrolyte flux (—)
prevent close-packing
Zn
Anode

**Fig. 4**

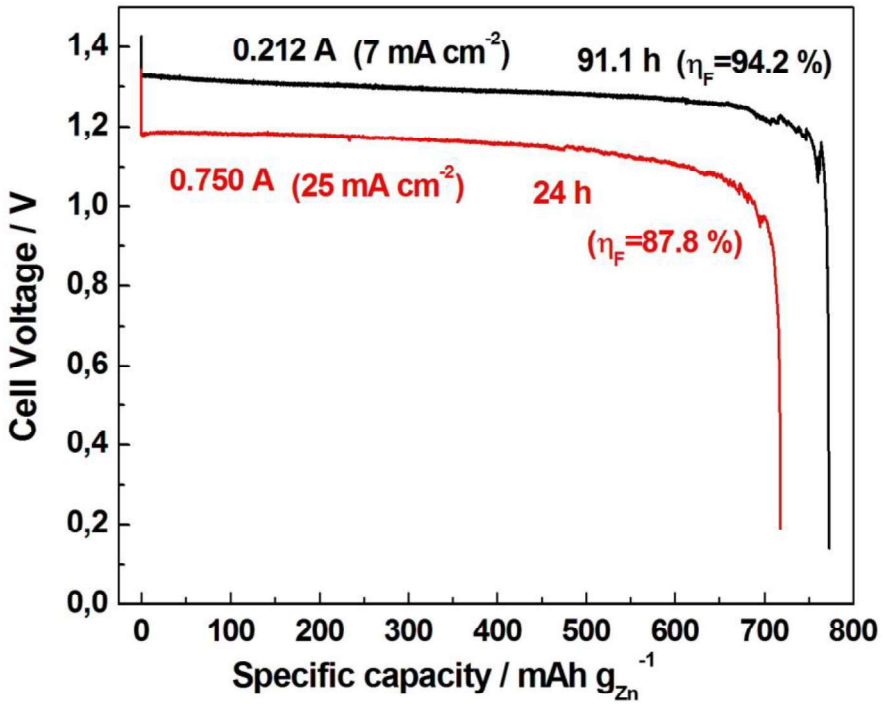
0.212 A (7 mA cm-2)
91.1 h (ηF=94.2 %)
0.750 A (25 mA cm-2)
24 h
(ηF=87.8 %)
Cell Voltage / V
Specific capacity / mAh gZn-1
1,4
1,2
1,0
0,8
0,6
0,4
0,2
0,0
0
100
200
300
400
500
600
700
800

**Fig. 5**

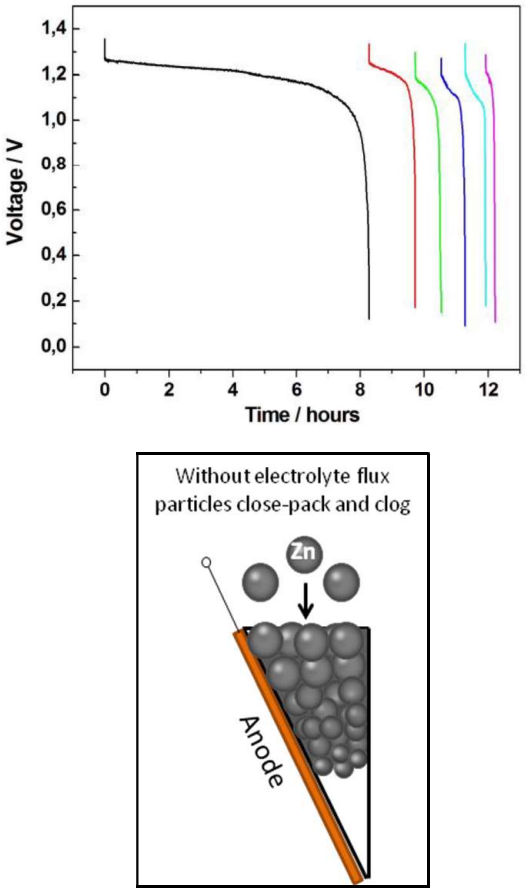
Voltage / V
1,4
1,2
1,0
0,8
0,6
0,4
0,2
0,0
0
2
4
6
8
10
12
Time / hours
Without electrolyte flux
particles close-pack and clog
Zn
Anode

**Fig. 6**

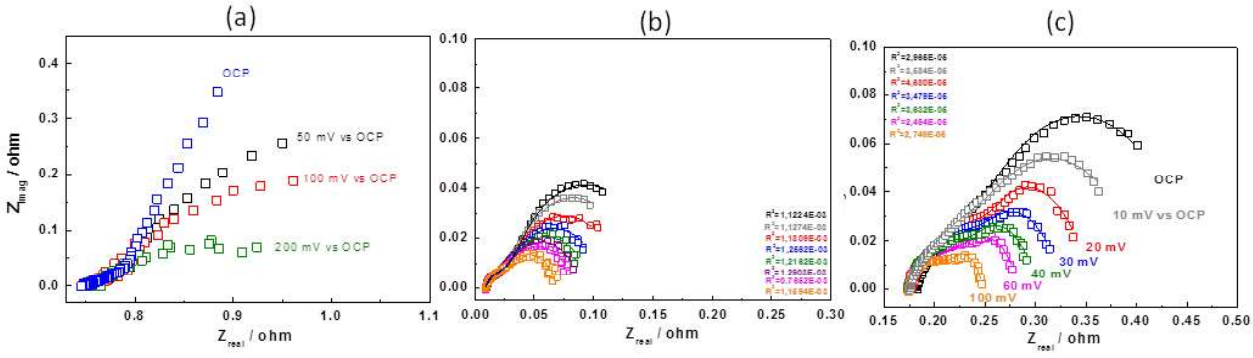
(a)
(b)
(c)
OCP
50 mV vs OCP
100 mV vs OCP
200 mV vs OCP
10 mV vs OCP
20 mV
30 mV
40 mV
60 mV
100 mV
Z_imag / ohm
Z_real / ohm

**Fig. 7**

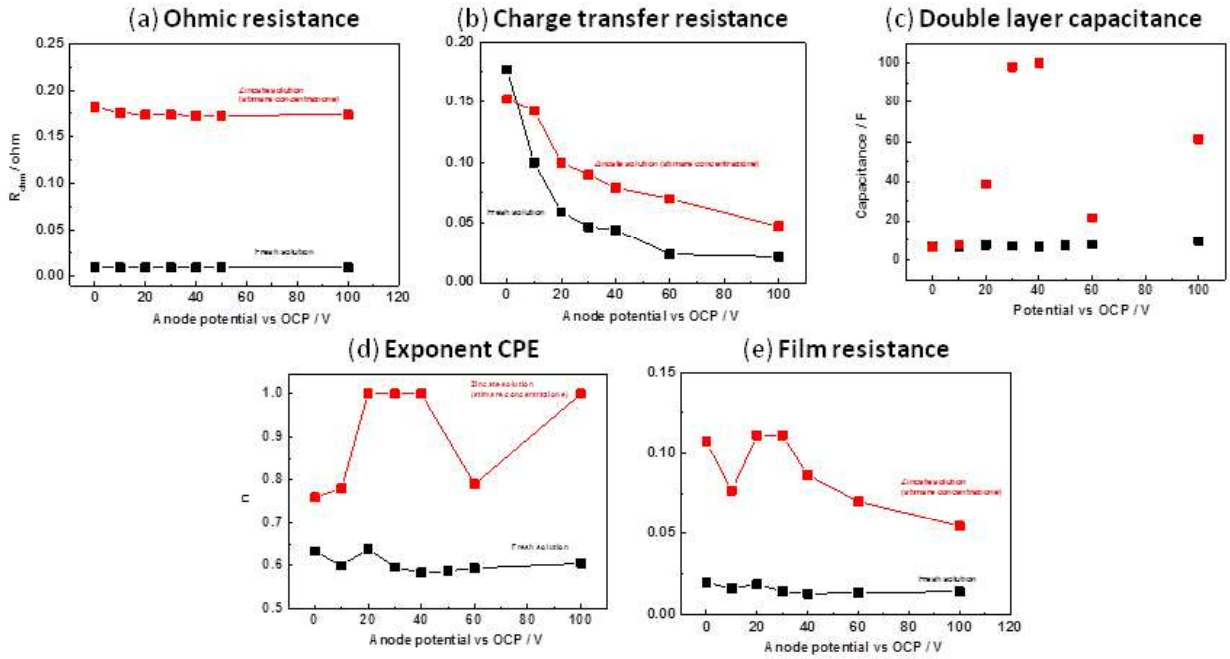
(a) Ohmic resistance
$R_{film}$ / ohm
Anode potential vs OCP / V
(b) Charge transfer resistance
Anode potential vs OCP / V
(c) Double layer capacitance
Capacitance / F
Potential vs OCP / V
(d) Exponent CPE
n
Anode potential vs OCP / V
(e) Film resistance
Anode potential vs OCP / V

**Fig.8**

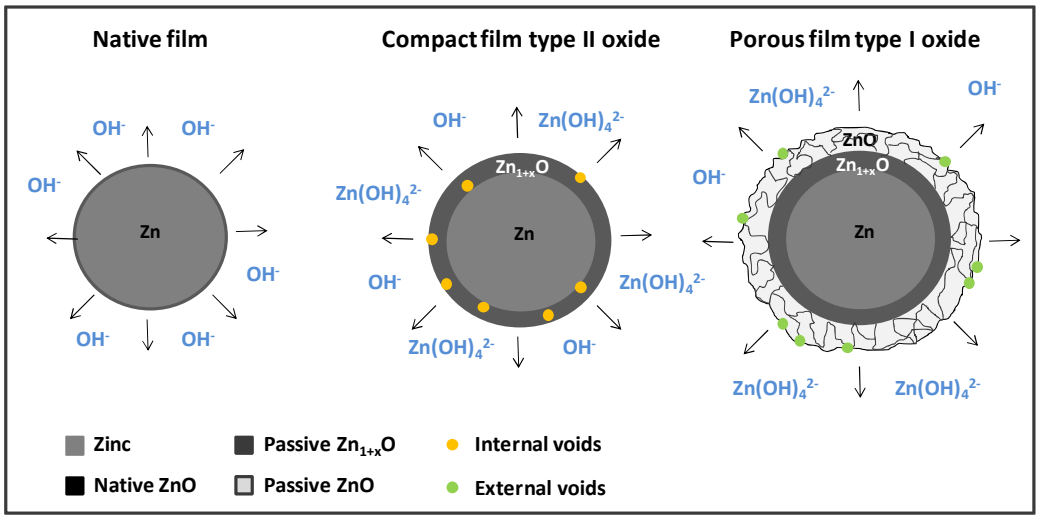
Native film
Compact film type II oxide
Porous film type I oxide
OH-
Zn
Zn(OH)4 2-
Zn1+xO
ZnO
Zinc
Native ZnO
Passive Zn1+xO
Passive ZnO
Internal voids
External voids

**Fig. 9**

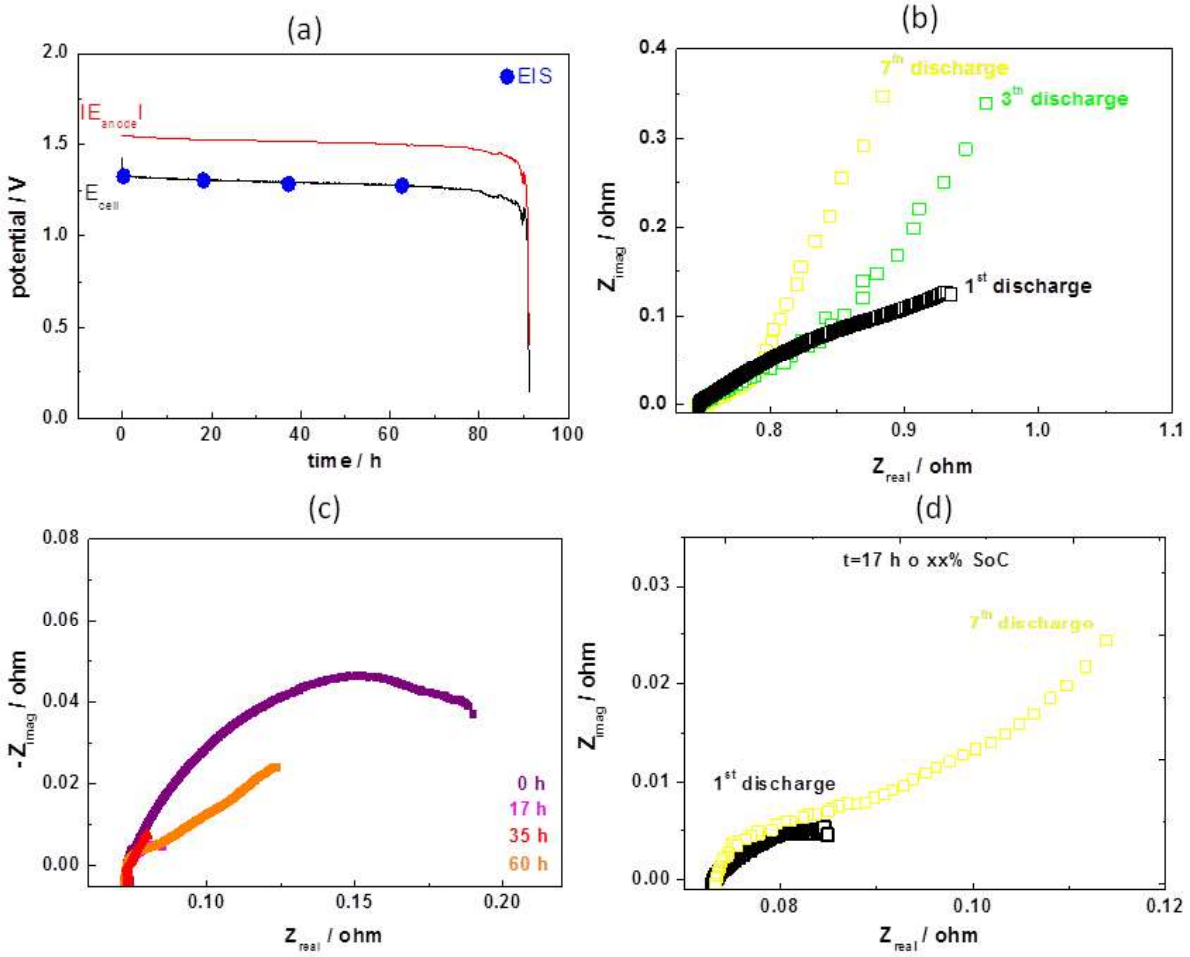
(a)
EIS
|E_anode|
E_cell
potential / V
time / h
(b)
7th discharge
3th discharge
1st discharge
Z_imag / ohm
Z_real / ohm
(c)
0 h
17 h
35 h
60 h
-Z_imag / ohm
Z_real / ohm
(d)
t=17 h o xx% SoC
7th discharge
1st discharge
Z_imag / ohm
Z_real / ohm

**Fig. 10**

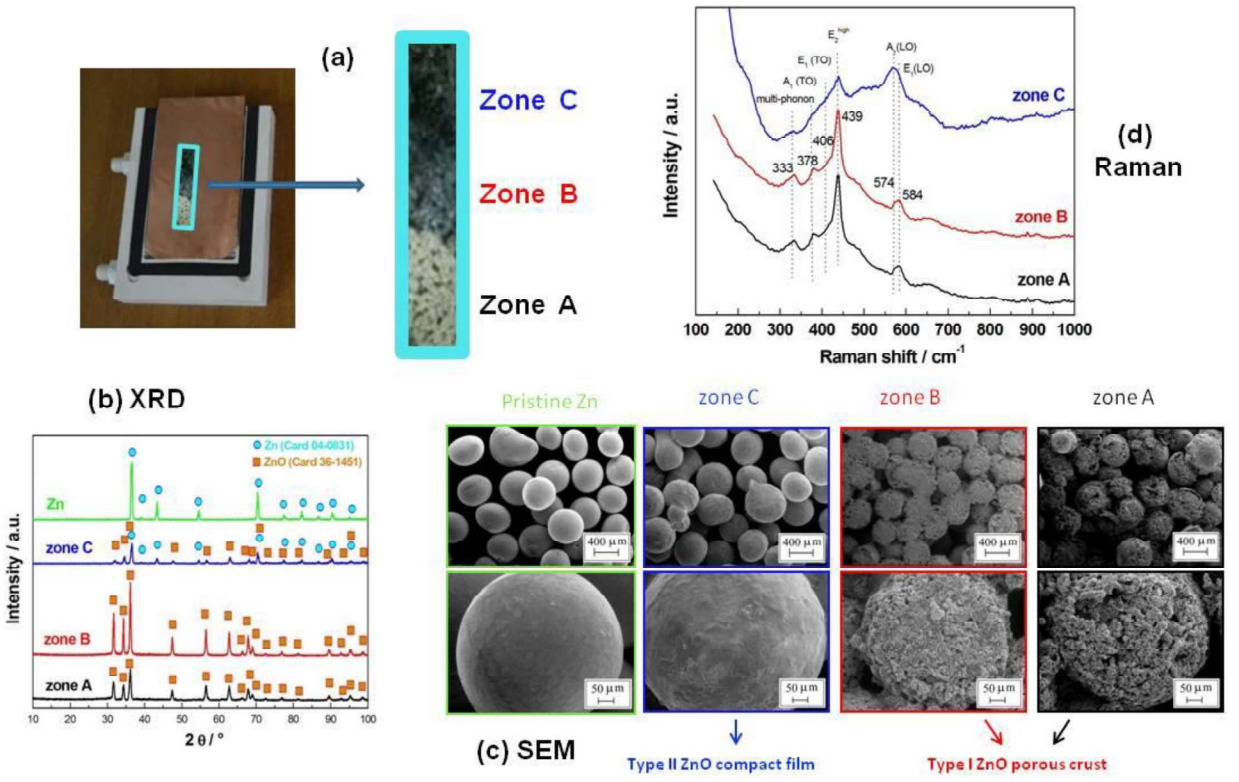
(a)
Zone C
Zone B
Zone A
(b) XRD
Zn (Card 04-0831)
ZnO (Card 36-1451)
Zn
zone C
zone B
zone A
Intensity / a.u.
2θ / °
(d) Raman
multi-phonon
zone C
zone B
zone A
439
406
378
333
574
584
Intensity / a.u.
Raman shift / cm-1
(c) SEM
Pristine Zn
zone C
zone B
zone A
400 μm
50 μm
Type II ZnO compact film
Type I ZnO porous crust

**Fig. 11**

Figure 1

Click here to download Figure Figure01.tif

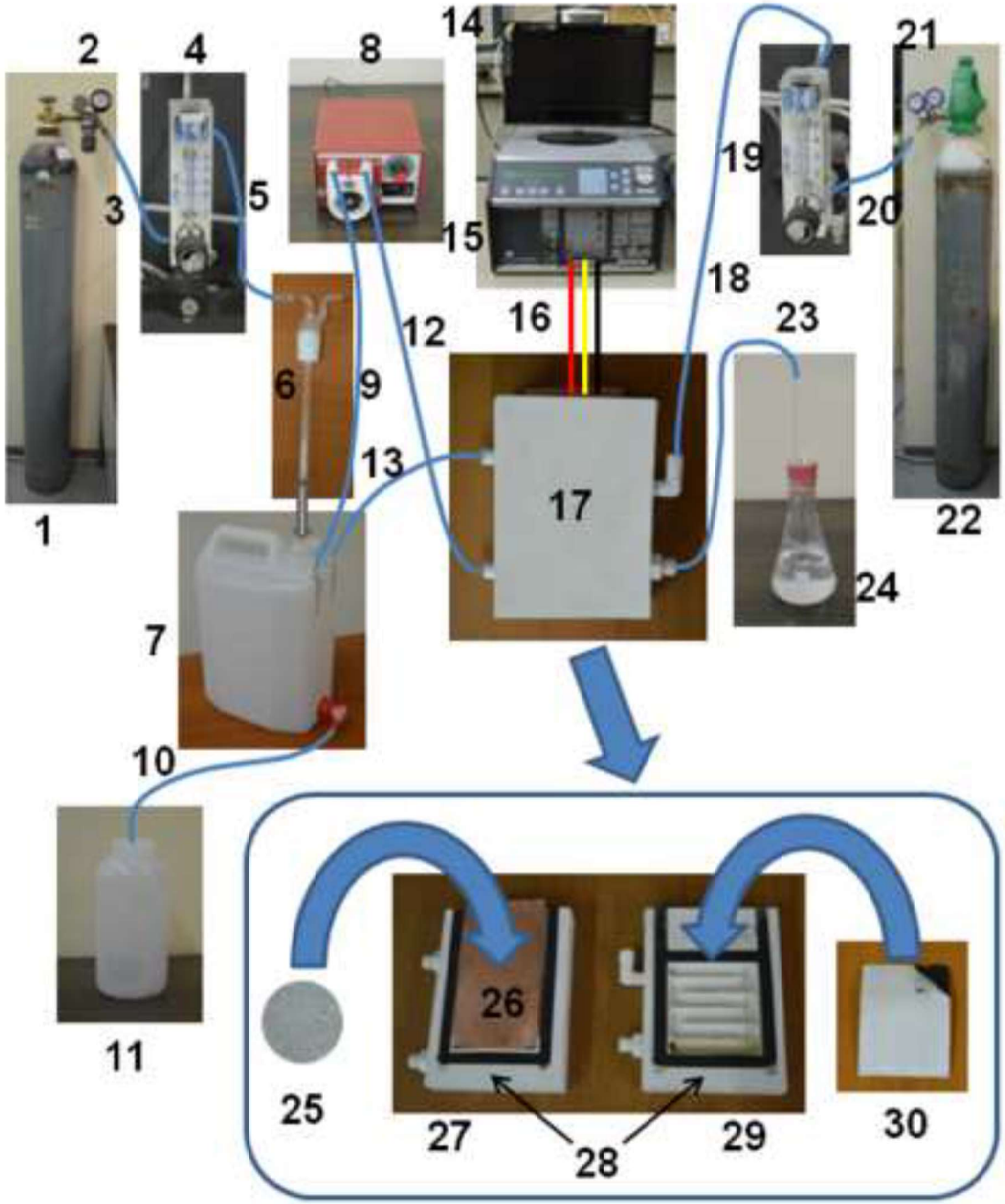


1. Nitrogen cylinder
2. Nitrogen gas flowmeter
3. Tygon tubing R-3603, Ø 6,4 mm
4. Gas flowmeter
5. Tygon tubing R-3603, Ø 6,4 mm
6. Gas bubbler
7. KOH storage tank
8. Peristaltic pump
9. Tygon tubing R-3603, Ø 6,4 mm
10. Tygon tubing R-3603, Ø 6,4 mm
11. Drain tank
12. Tygon tubing R-3603, Ø 6,4 mm
13. Tygon tubing R-3603, Ø 6,4 mm
14. PC interfaced with the potentiostat/galvanostat
15. Potentiostat/galvanostat
16. Potentiostat/galvanostat cables
17. PMMA cell
18. Tygon tubing R-3603, Ø 6,4 mm
19. Gas flowmeter
20. Tygon tubing R-3603, Ø 6,4 mm
21. Oxygen gas flowmeter
22. Oxygen cylinder
23. Tygon tubing R-3603, Ø 6,4 mm
24. Trap for checking $O_2$ flow
25. Zinc spheres anode
26. Copper current collector
27. Hopper (anodic side of the cell)
28. Gaskets
29. Gas distribution plate (cathodic side of the cell)
30. Air cathode

Figure 2

Click here to download Figure Figure02.tif

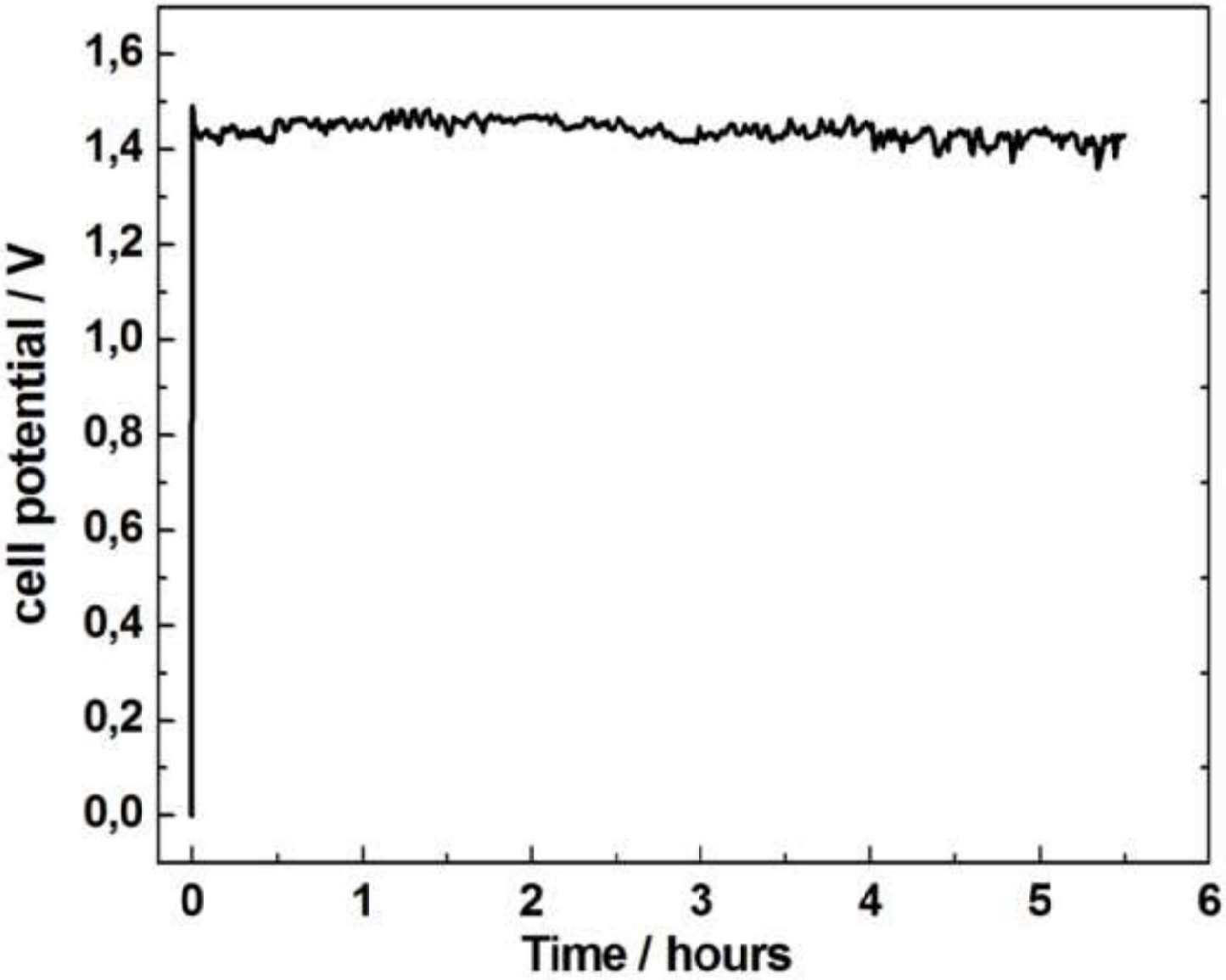

Figure 3

Click here to download Figure Figure03.TIF

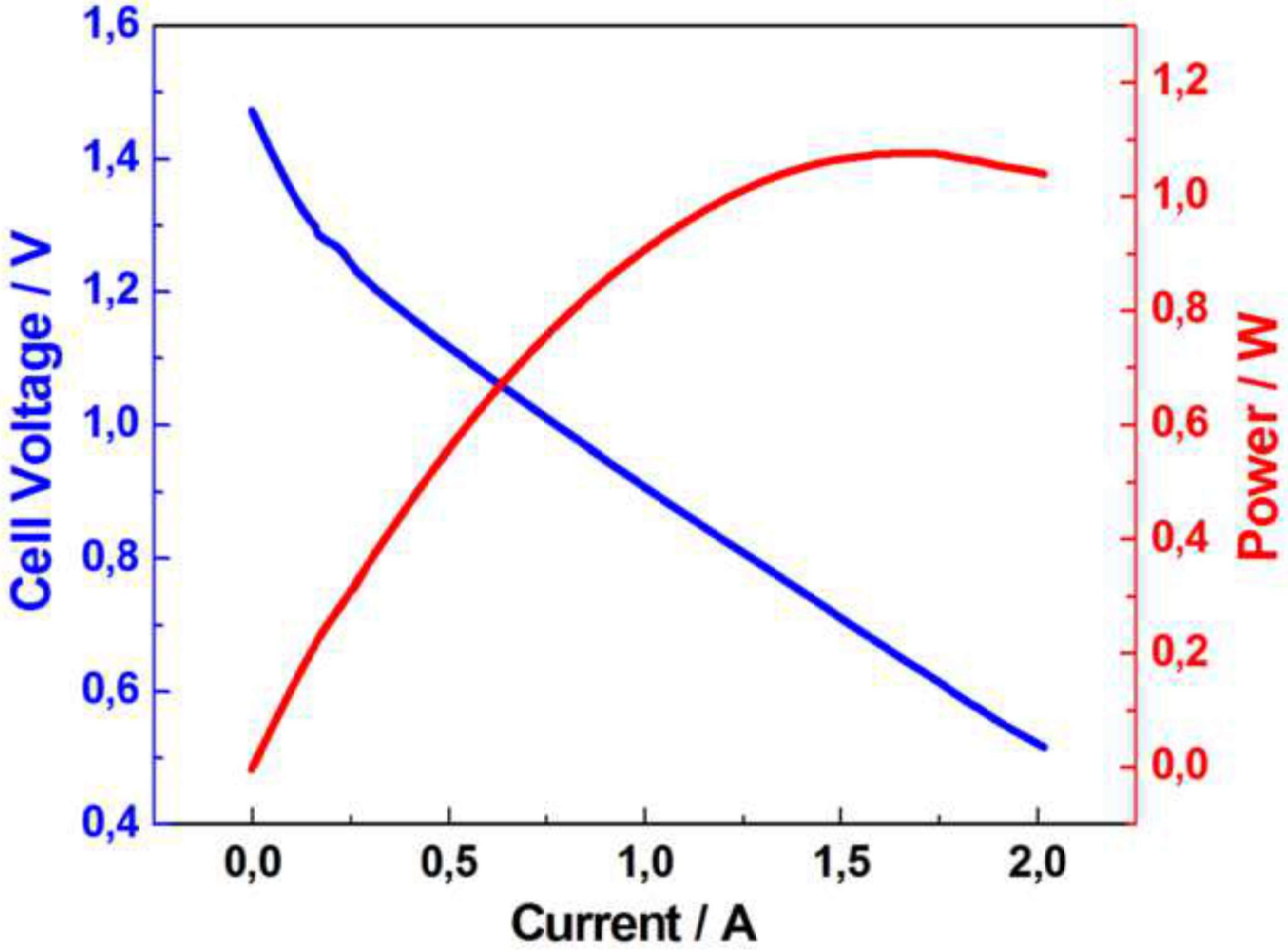

Figure 4a

Click here to download Figure Figure04a.TIF

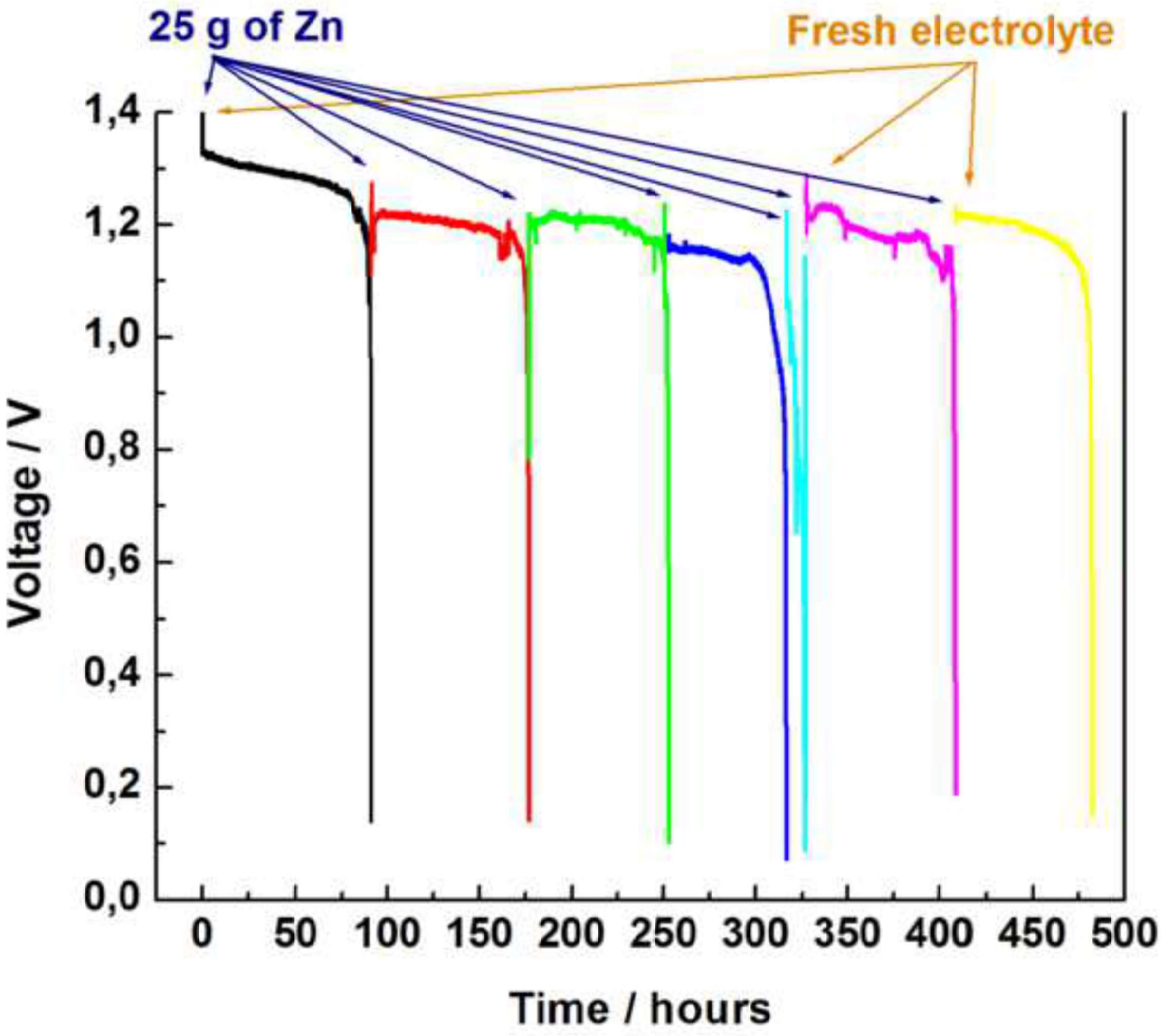

Figure 4b

Click here to download Figure Figure04b.TIF

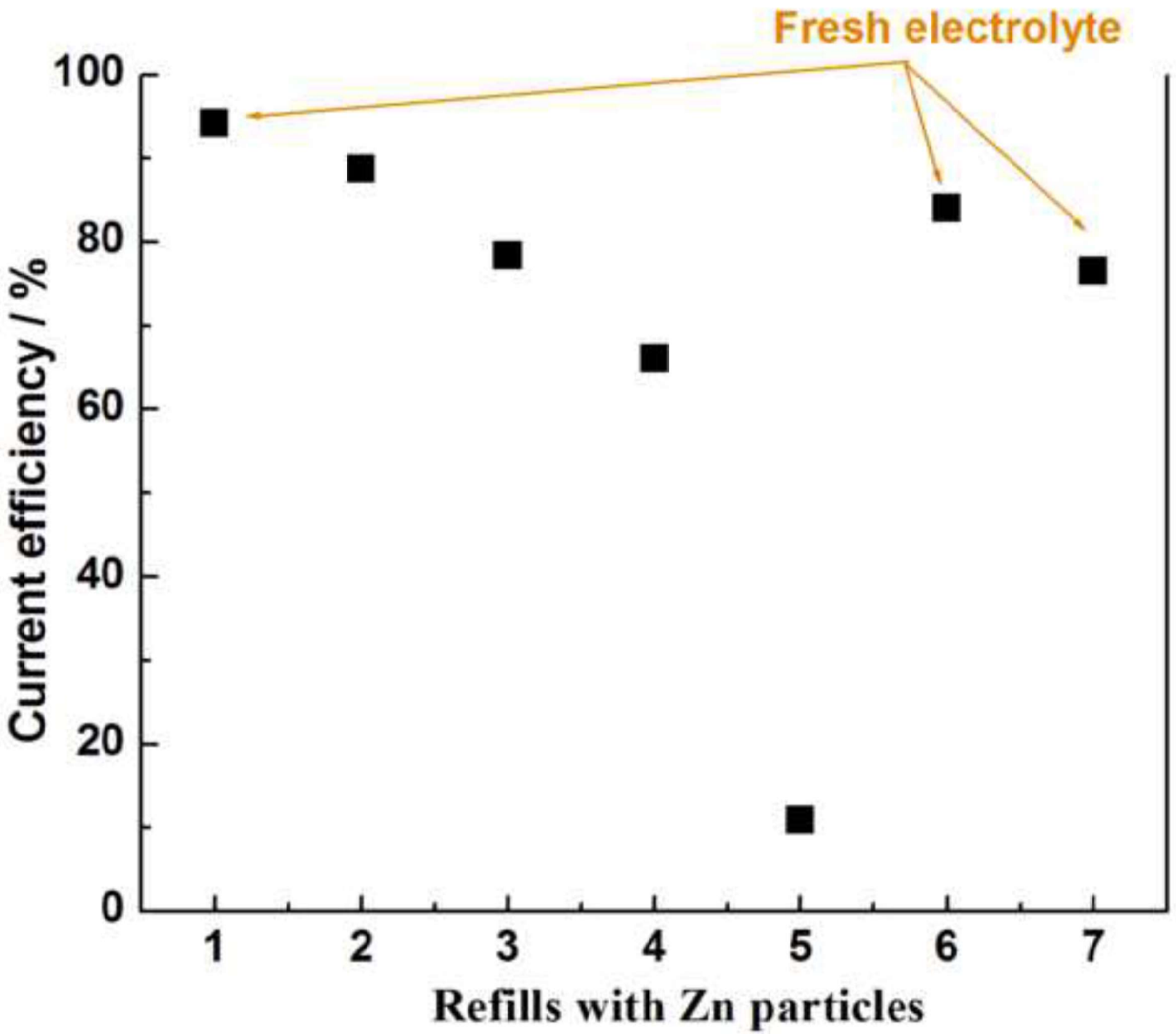

Figure 4c

Click here to download Figure Figure4c.tif

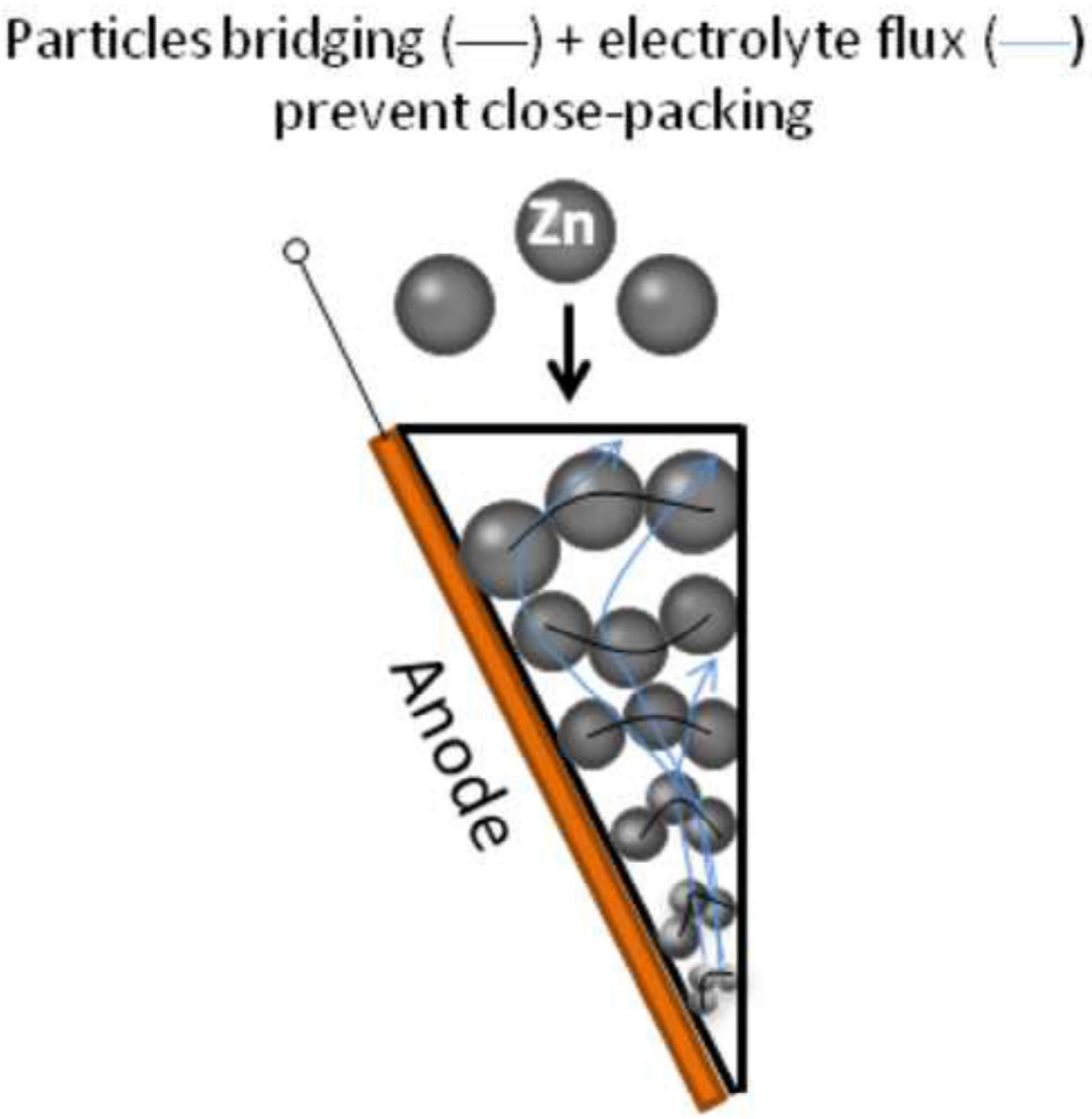

Figure 5

Click here to download Figure Figure05.TIF

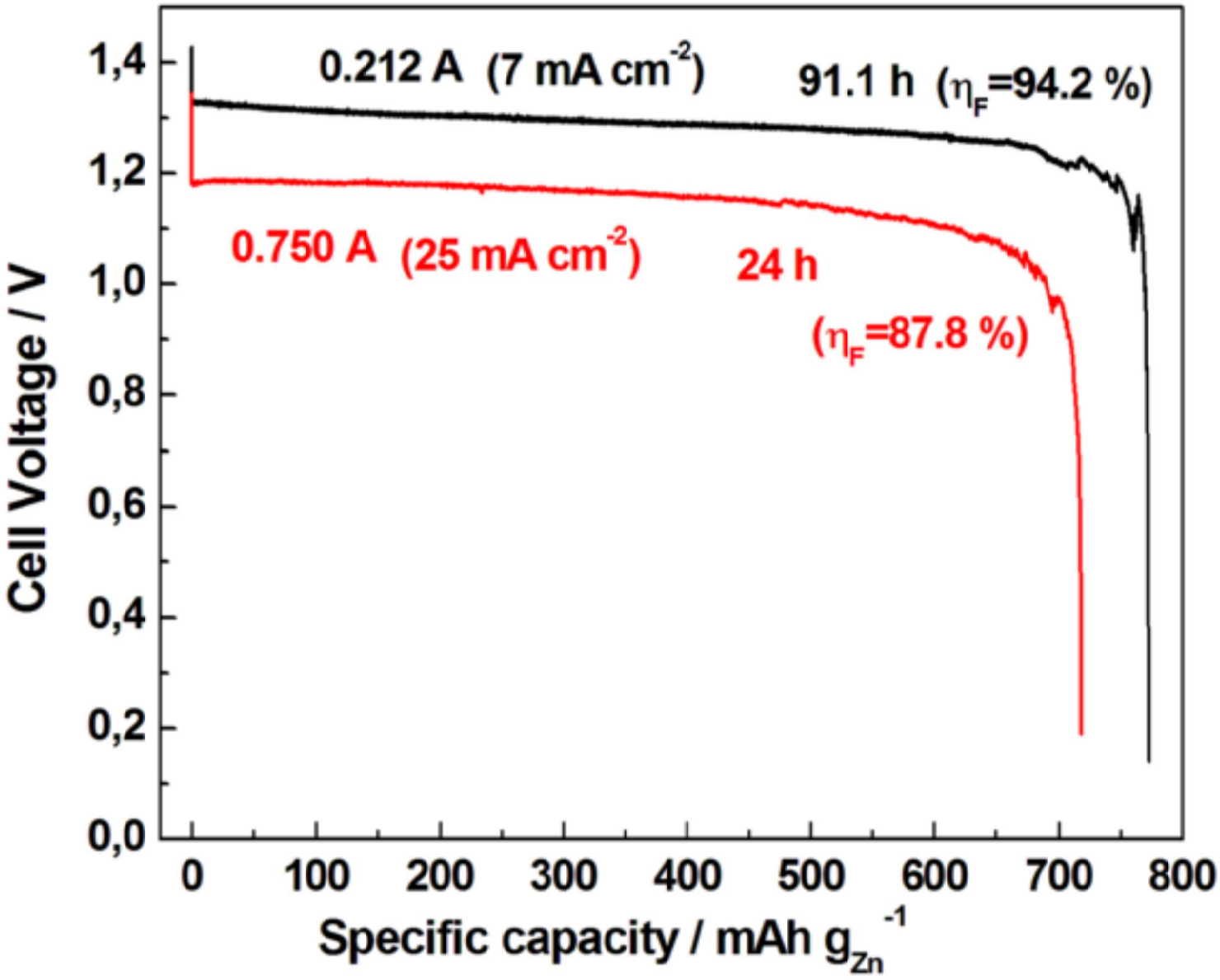

Figure 6a

Click here to download Figure Figure06.TIF

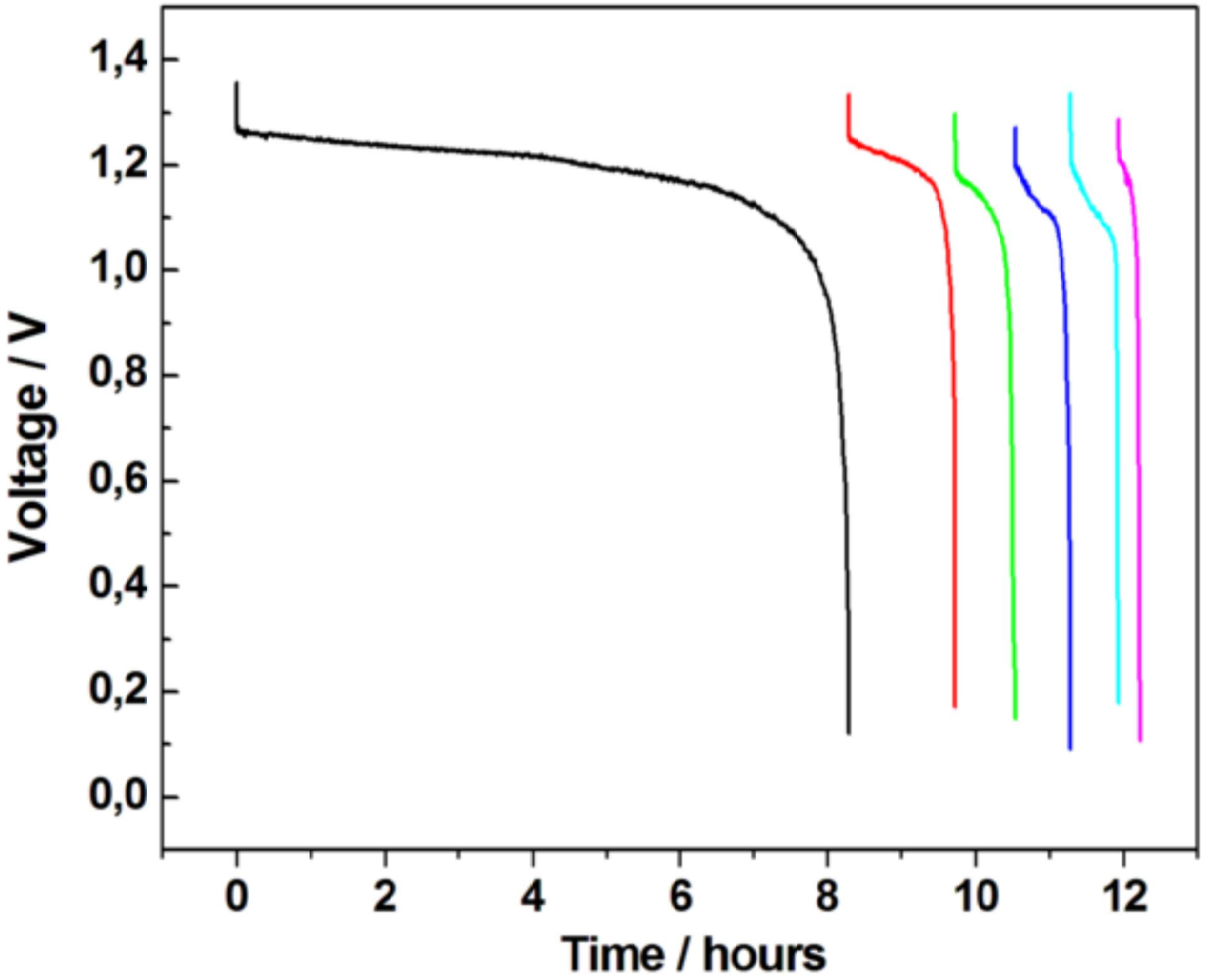

Figure 6b

Click here to download Figure Figure06b.tif

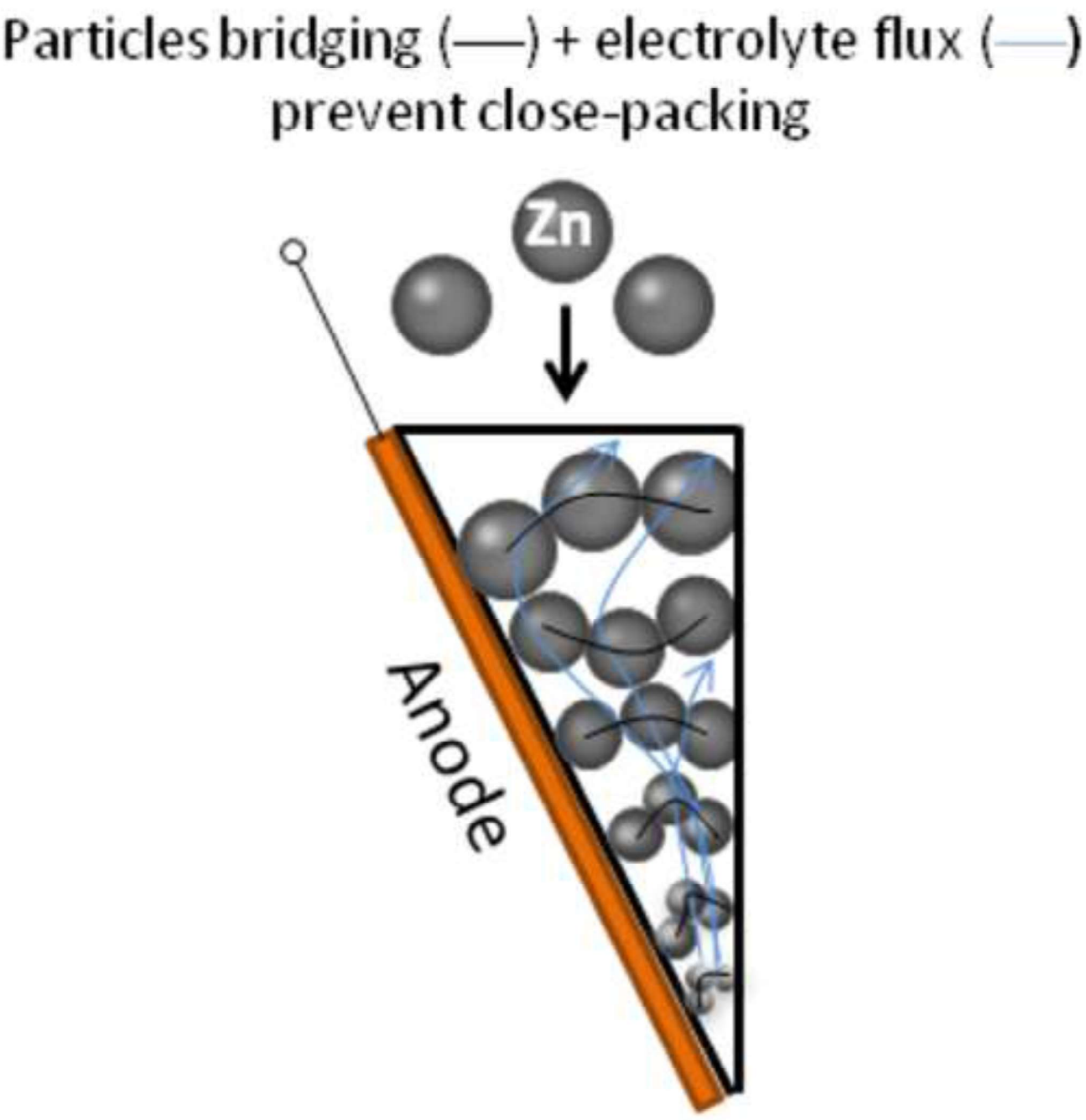

Figure 7

Click here to download Figure Figure07.tif

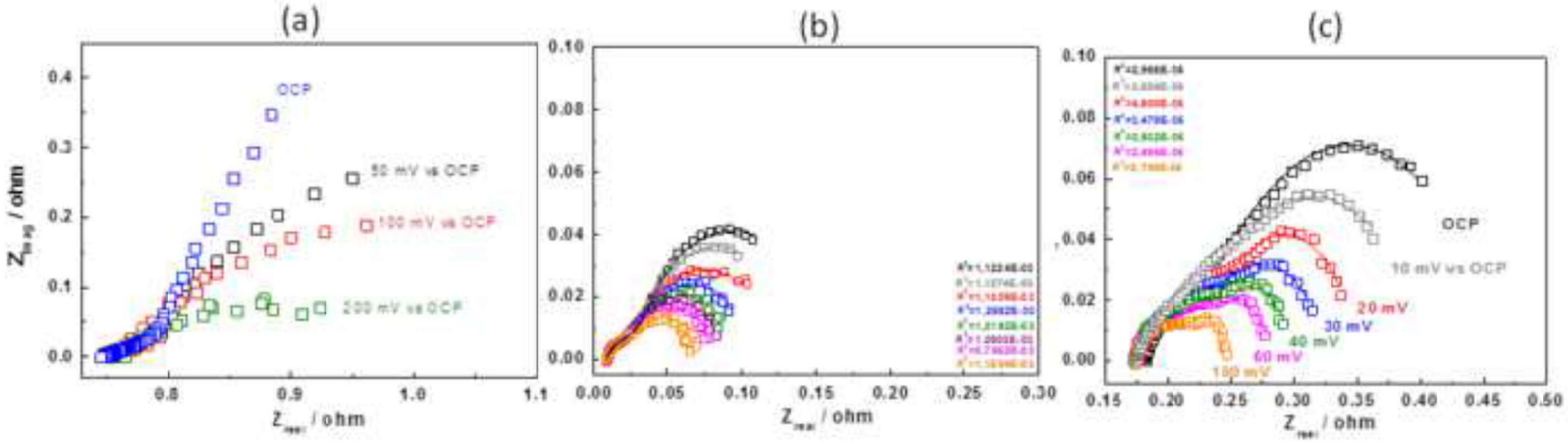

Figure 8

Click here to download Figure Figure08.tif

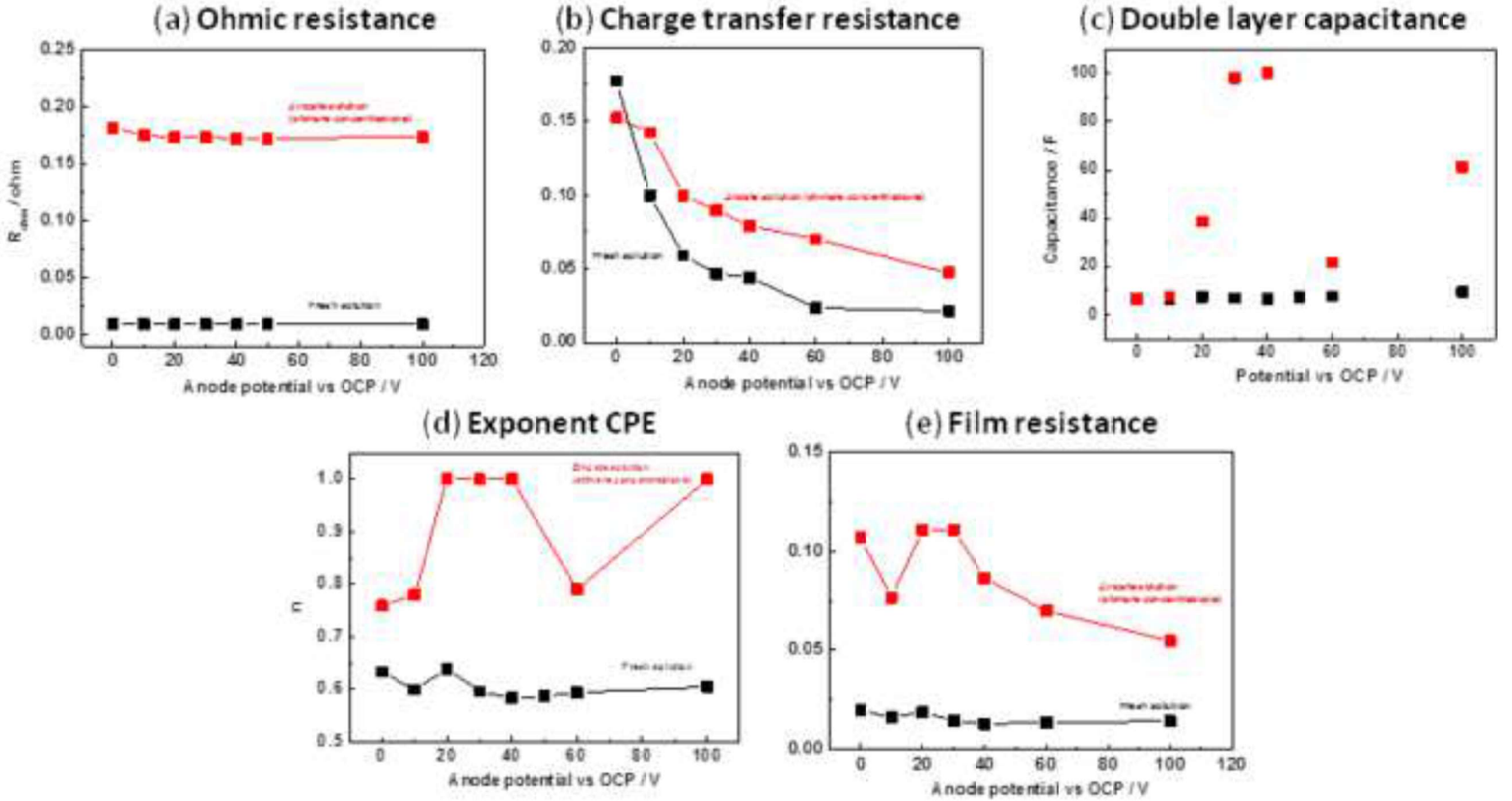

Figure 9

Click here to download Figure Figure09.tif

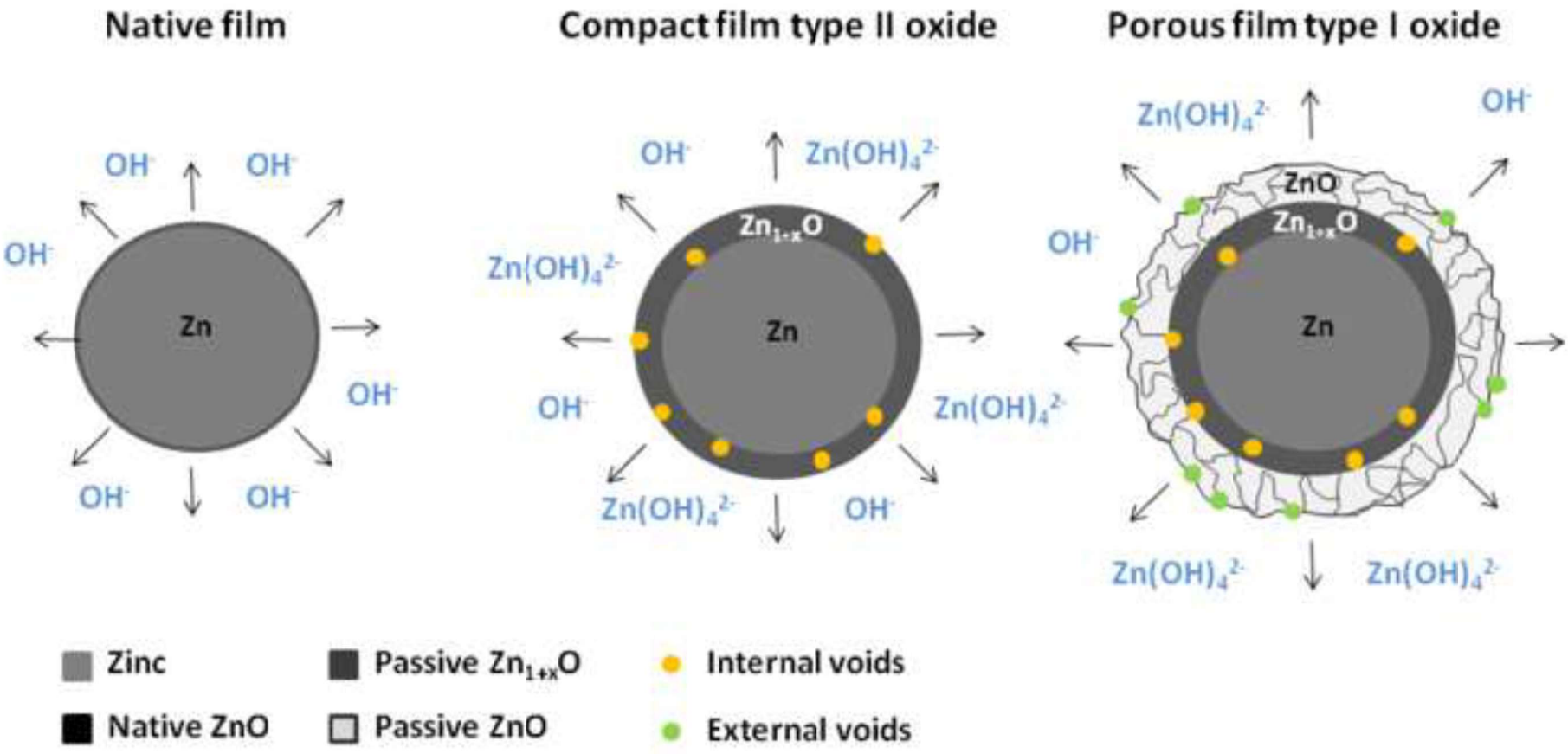

Figure 10

Click here to download Figure Figure10.tif

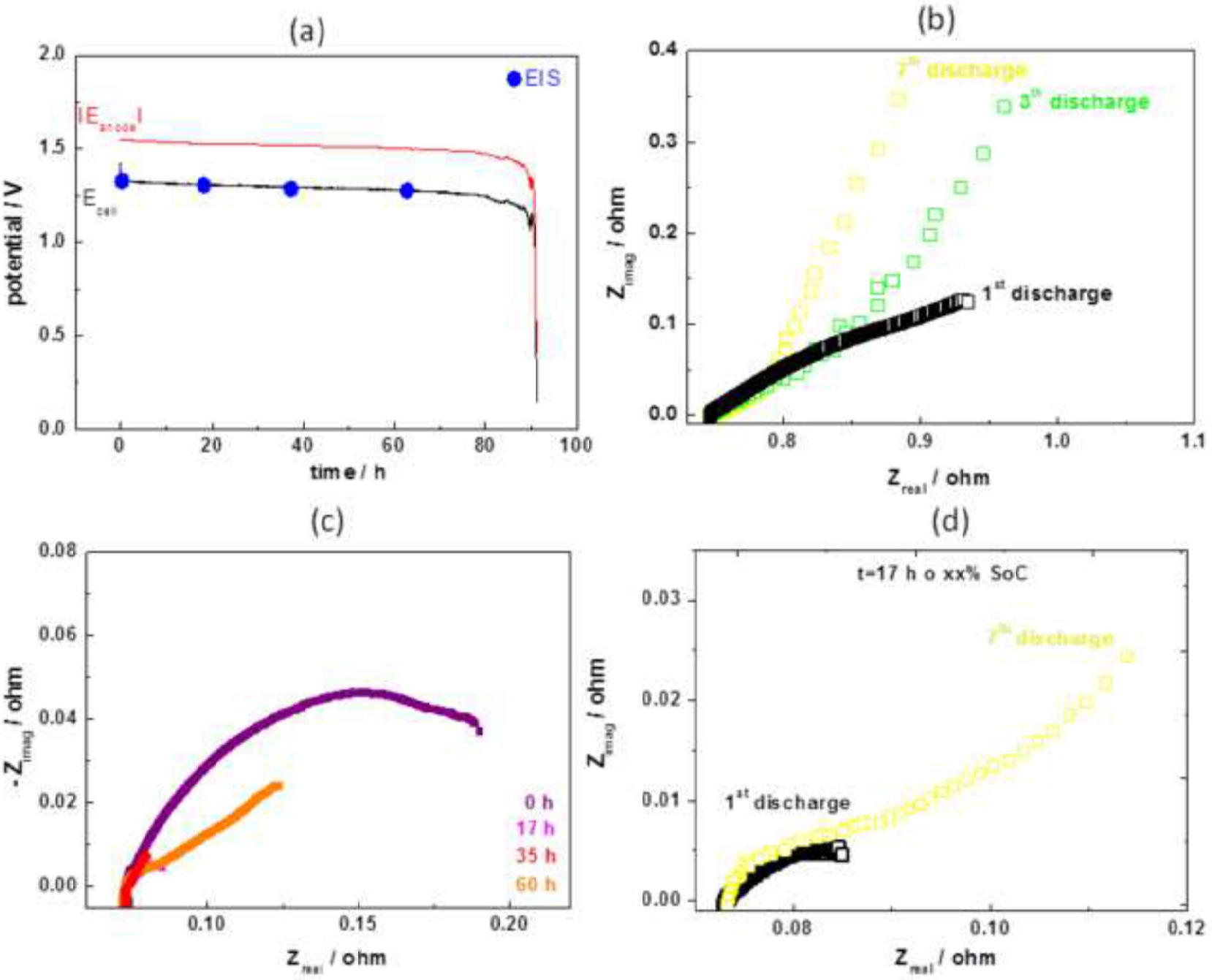

Figure 11

Click here to download Figure Figure11.tif

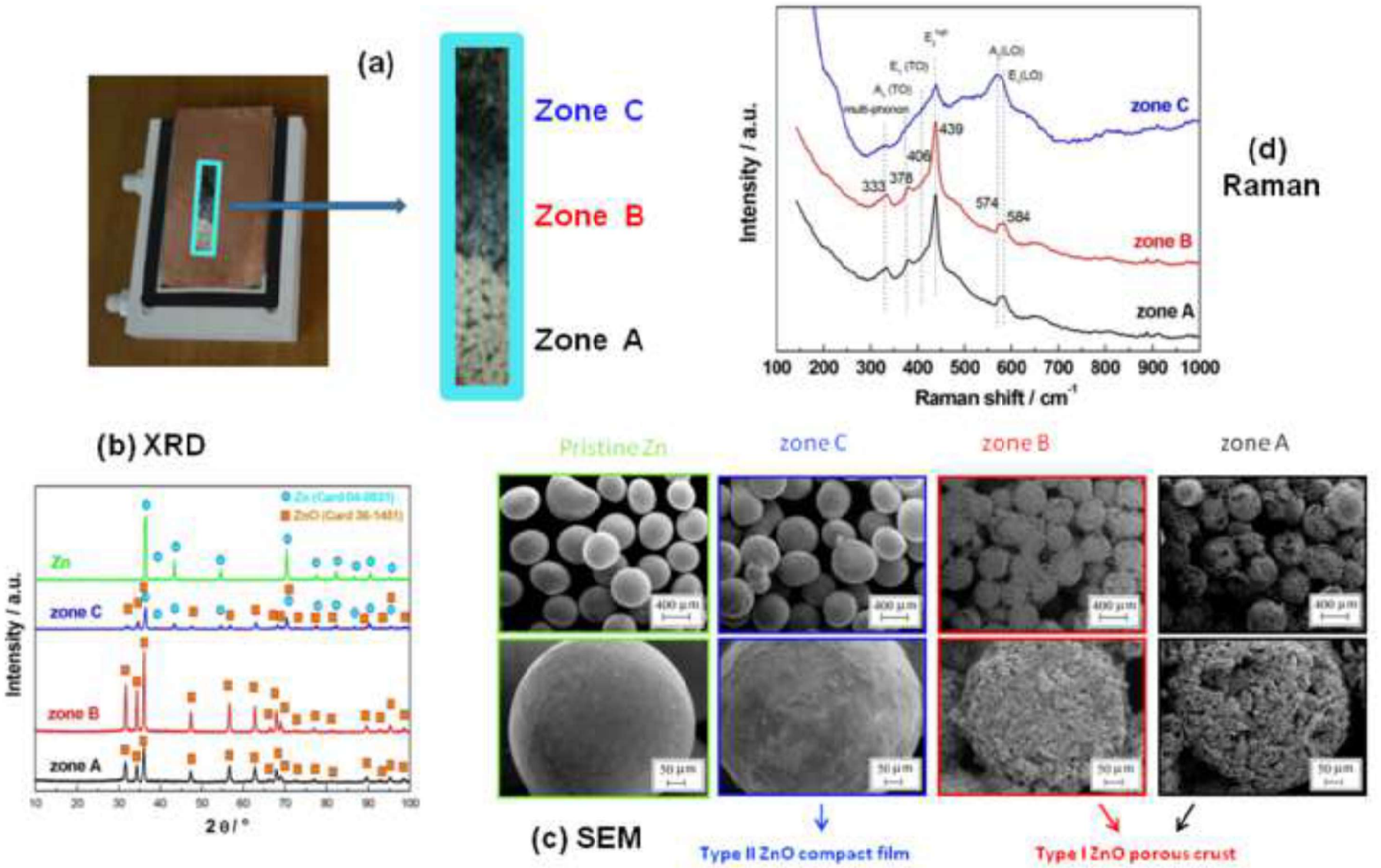

Graphical Abstract

Click here to download Graphical Abstract Graphical abstract.tif